Controlling flood displacement fronts using a parallel analytical streamline simulator

Ruud Weijermars [a,*], Arnaud van Harmelen [a,b], Lihua Zuo [a]

[a] Harold Vance Department of Petroleum Engineering, Texas A&M University, 3116 TAMU College Station, TX 77843-3116, USA
[b] Department of Applied Mathematics, Delft University of Technology, Mekelweg 4, Delft 2628CD, The Netherlands

ABSTRACT

The Analytical Element Method (AEM), originally developed for mathematical modeling of groundwater flow, is here applied in closed-loop waterflood simulations. The Parallel Analytical Streamline Simulator (PASS), based on AEM, enables fast time-of-flight (TOF) calculations and visualizations of sweep efficiency in homogeneous, heterogeneous and fractured reservoirs. Simulations with PASS can test the sweep efficiency for a wide range of well patterns even before field development. We assume a simple direct-line drive and various initial reservoir attributes: a homogenous base case and further explore the effects on the flood advance of zones with heterogeneous permeability and an impervious fault. For all cases, analytical streamline patterns and time-of-flight contours for the flood front (obtained with PASS) are compared to those generated via an independent method based on numerical discretization by a commercial reservoir simulator. The results are convergent and confirm that PASS can be used to determine in closed-loop simulations the well rates that will avoid the occurrence of premature water breakthrough in the production wells. Early breakthrough in the homogenous reservoir occurs for the central producers and occurs later for the peripheral producers. Real-time adjustments of the water injection rates based on closed-loop surveillance of the pressures in producer wells can redirect and control the reservoir flow such that the floodfront arrives simultaneously at all producers. For the heterogeneous reservoir, smart-field well-control for improved sweep efficiency is also visualized. However, when an impervious fault zone blocks the flow path between injector and producer wells the occurrence of premature arrival of injection water in some producers cannot be avoided.

© 2015 Elsevier B.V. All rights reserved.

1. Introduction

Effective waterflood management begins with optimization of the well architecture design to establish the most effective well constellation to achieve the largest net cash flow from a certain field. Integrated over time, the maximum net cash flow generates a corresponding maximum net present value over the lifecycle of the field. Reservoir models in early field life are commonly based on few subsurface data and become more accurate when more data on field performance accumulate over time. Determining the optimum well patterns, borehole orientation and locations, as well as the actual number of wells will result in a higher NPV (e.g., refs. in Zandvliet, 2008). Testing multiple scenarios for a range of well architectures under geological uncertainty is possible with our Parallel Analytical Streamline Simulator (PASS). The present proof-of-concept study focuses on a simple dynamic optimization for a given well pattern and assumes a number of synthetic reservoir attributes to benchmark results and to demonstrate how well-rate adjustments can control and redirect the flood front.

The simulator developed by us is based on the Analytical Element Method (AEM), previously used in groundwater flow studies (Strack, 1989; Haitjema, 1995). The basic philosophy of AEM makes use of the analytical elements described by complex potentials. This study uses a subset of such analytical elements and demonstrates the potential merit for closed-loop reservoir modeling and flow visualizations. All integrals in the AEM are based on linear partial-differential equations which are analytically obtained. Many of these equations cannot be solved practically without the aid of modern computing power. The AEM differs from the finite difference and finite element methods in that the former does not rely upon discretization of volumes or areas in the modeled system; only internal and external boundaries are discretized. The strength of the AEM is its foundation in analytical descriptions that require only few input parameters to model a broad range of flow scenarios. The acquisition of detailed reservoir data by geological

and geophysical methods is costly, which is why reservoir response studies based on fast streamline simulations with PASS can help guide the selective acquisition of subsurface data to improve field performance even before drilling the actual wells.

Early reservoir descriptions based on complex potentials have simplified spatial variations in reservoir properties. For example, Muskat (1949 a,b) extended his line integral method to account for reservoir heterogeneity by assuming that varying the layer thickness is equivalent to specifying a spatial permeability gradient. A more advanced approach makes use of integrated line sources and sinks (line dipoles and line doublets), which can be collated to delineate reservoir sub-domains of different permeability using analytical elements to create closed boundaries (Strack, 1989). The AEM approach was more recently applied to model reservoir flow patterns and pressures in synthetic well models (Fokker et al., 2005; Fokker and Verga, 2008). However, the latter models did not consider any closed-loop response simulations. The application in our study advances the AEM in that direction.

Certain analytical tools used in AEM have previously been applied to model particular aspects of hydrocarbon flow in the early days of automated computing power development. However, processing speed was limited and processor cost so high that computer-aided streamline solutions using linear partial-differential equations based on complex potentials could only be afforded by a limited number of corporate developers. For example, Doyle and Wurl (1971) used a $2 million UNIVAC11008 developed by Sperry Rand Corporation to model analytically with potential functions the waterflood performance of an oil field in northeast Texas. The field, bounded by faults on all sides, was modeled using the method of image wells to ensure that streamlines conformed to the fault boundaries. Similarly, Higgins and Leighton (1974) used a $7 million CDC6600 mainframe computer developed by Control Data Corporation (with just enough memory when it became available in the 1960s) to compute the line integrals for flow in sub-domain layers of their reservoir model. The costly method was merited at the time because field performance and reservoir models could be compared in order to improve waterflood performance. History matching was applied to improve the model parameterization and enhance the accuracy of the production forecast for the second half of the field life-cycle.

Over the past 5 decades, the cost of computation time has come down at least three orders of magnitude. Most modern desktop computers have now enough processing power to run flow simulations based on complex potentials. Previous limitations of the complex potential method itself have also been overcome. For example, extensions of analytical to semi-analytical streamline solutions have been documented in numerous studies (Sato and Horne, 1993a,b; Sato and Watanabe, 2004; Hazlett et al., 2007; Sato, 2015). Such extensions allow for streamline simulations accounting for, a.o., finite reservoir boundaries, internal heterogeneity and anisotropy. In spite of these developments, commercial reservoir modeling tools based on finite difference techniques remain the principal tool used by industry in the optimization of production output and net present value (NPV) for at least a certain type of assets (see Section 2.1). The present study advocates that the expanding range of reservoir modeling tools all have their specific merits. For example, analytical models can be employed for generating conceptual insight and for instructional purposes, as well as in practical applications because of their transparency, speed and versatility.

This article is organized as follows. Section 2 places streamline-based reservoir models in a broader context and outlines the analytical element method and key algorithms used to develop our streamline simulator (tailor-made in this study for 2D water-flooding applications). Section 3 details the basic assumptions. Section 4 applies the simulator to synthetic examples and

benchmarks the results against streamline simulations rendered with a numerical simulator (combining ECLIPSE, DESTINY and Petrel data). A discussion and conclusions are given respectively in Sections 5 and 6.

2. Tools and methods

2.1. Streamline simulation merits

The petroleum industry strives to develop the most sophisticated tools to validate field development decisions. Appropriate estimations of the hydrocarbon reserves categories are at the foundation of investment decisions, which is why a range of tools and methods is available for estimating hydrocarbon reserves (Fig. 1). The proved reserves are based on a proven recovery technology and the resource recovery profile is determined using a field development concept. Investments must meet the threshold of economic returns using certain commodity price scenarios applied to an estimation of the reserve volumes. Integrated production models are the ultimate state-of-the-art (Fig. 1, top), and other reservoir modeling tools carry the risk of compromising technical rigor (which reviewers of our paper frequently reminded us). Streamline-based methods, like any model tool, indeed have limiting assumptions but these need not compromise technical rigor when the proper tool (or a combination of tools) is applied to the proper asset. Streamline-based history matching and well simulations are part of the larger tool box currently available for modeling hydrocarbon recovery optimization. The hierarchy of modeling tools to evaluate the reserve volumes in a particular hydrocarbon reservoir can be summarized as follows (Fig. 1):

1. *Analogy methods* are mostly used for estimation of prospect size before drilling and for proved undeveloped reserves in outstep and infill drilling locations observing the limiting spacing units.
2. *Volumetric methods* are used in early field life when no or only limited production data are available. Oil and gas in place are estimated using 3D reservoir characterization based on detailed geological, petrophysical (logs) and geophysical data (seismic).
3. *Material balance methods* use early production data to obtain reserve estimations by assuming production is maintained by a linear pressure decline until the economic limit is reached.
4. *Decline curve analysis* prevails as the principal tool [based on the early work of Arps, 1945] for estimating the productivity of single and multiple wells of unconventional reservoir rocks as a basis for estimations of the natural gas and liquids reserves. History matching is used to continually update the production
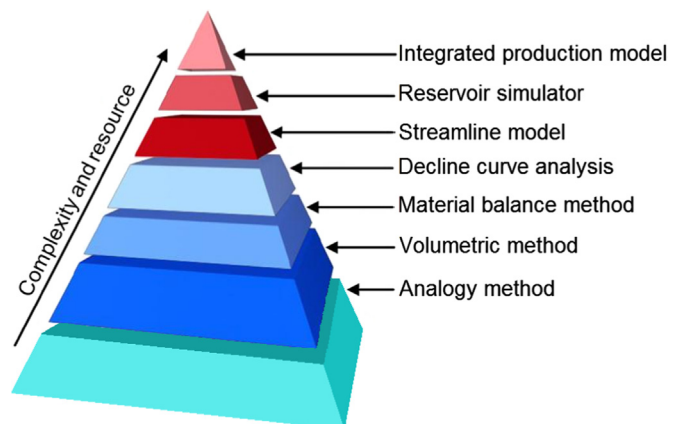

Fig. 1. Hierarchy of common methods employed for hydrocarbon reserves estimation. Adapted from Browning et al. (2012), after Pande (2005).

type curves that commonly fit a hyperbolic decline curve. The economic limit criteria truncate the sub-economic well rates.

5. *Streamline models* can be used for a variety of conventional reservoirs produced with water, steam or gas injection for improved recovery and pressure maintenance. Multiple scenarios are tested to establish which well configuration delivers the best sweep (best drainage) using the fluid flux along streamtubes to achieve maximized connections between injectors and producers. Such models can be used as standalone applications or provide input to reservoir simulators with a broader capacity.

6. *Reservoir simulators* can solve for the spatial distribution of saturations and pressures over time as a function of PVT fluid properties, permeability and porosity distributions and structural topology of the reservoir. Ideally, such models account for multi-phase flow and pressure dependency of oleic, gas and water phase appearance and effects on miscibility of the three components (oil, gas, water). Reservoir models require huge number of input data and commonly are employed to develop larger conventional onshore and offshore assets.

7. *Integrated production models* are reservoir simulators that are coupled with the physical constraints of surface facilities, which are particularly relevant for ultra-deep water projects. Fluid properties may change rapidly in risers and the PVT conditions affect the pump scenarios of the wells (Browning et al., 2012).

Streamline simulations tools are thus placed in context. In domains of increased geological complexity with variable physical reservoir properties and conditions, streamline simulators can provide important support to finite difference (FD) reservoir simulators by identifying the reservoir sections where the most complex flow paths occur for a particular well architecture (Datta-Gupta and King, 2007). Streamline simulators can quantify the time-of-flight (TOF) and areal sweep efficiency (E_A), and unlike FD models, do not suffer from numerical dispersion, mitigation of which requires finer grid-resolution in FD methods, which increases the model complexity and computation time. For example, PASS can help identify injector partitions, well-pair connections, swept regions, oil withdrawal regions and time of flight. All these elements are highlighted in Fig. 2 for clarity. Analytical streamline simulations based on AEM are suitable for fast studies of reservoir sweep such as advocated in fast flow-diagnostics (Møyner et al., 2015; Natvig and Lie, 2008) and fast-marching methods for visualization of well drainage of fractured reservoirs (Zhang et al., 2013).

2.2. Analytical element method

The analytical element method (AEM) is applied in this study to systematically show the impact of some of the transmissibility variations on reservoir flow. Reservoir transmissibility can be highly heterogeneous due to permeability variations, heterogeneous permeability zones, and discrete obstructions such as impermeable faults, conductive cracks, and leaky fractures (with fluid loss/gain). The occurrence of such geological features obviously affects the hydraulic resistance experienced by fluids flowing in a porous reservoir. Fluid flow in reservoirs with varying physical properties can be described by analytical boundary integrals. This method was originally restricted to 2D flow problems (Strack, 1989) but can be expanded to 3D flow descriptions (Haitjema, 1995). The method uses analytical, closed-form
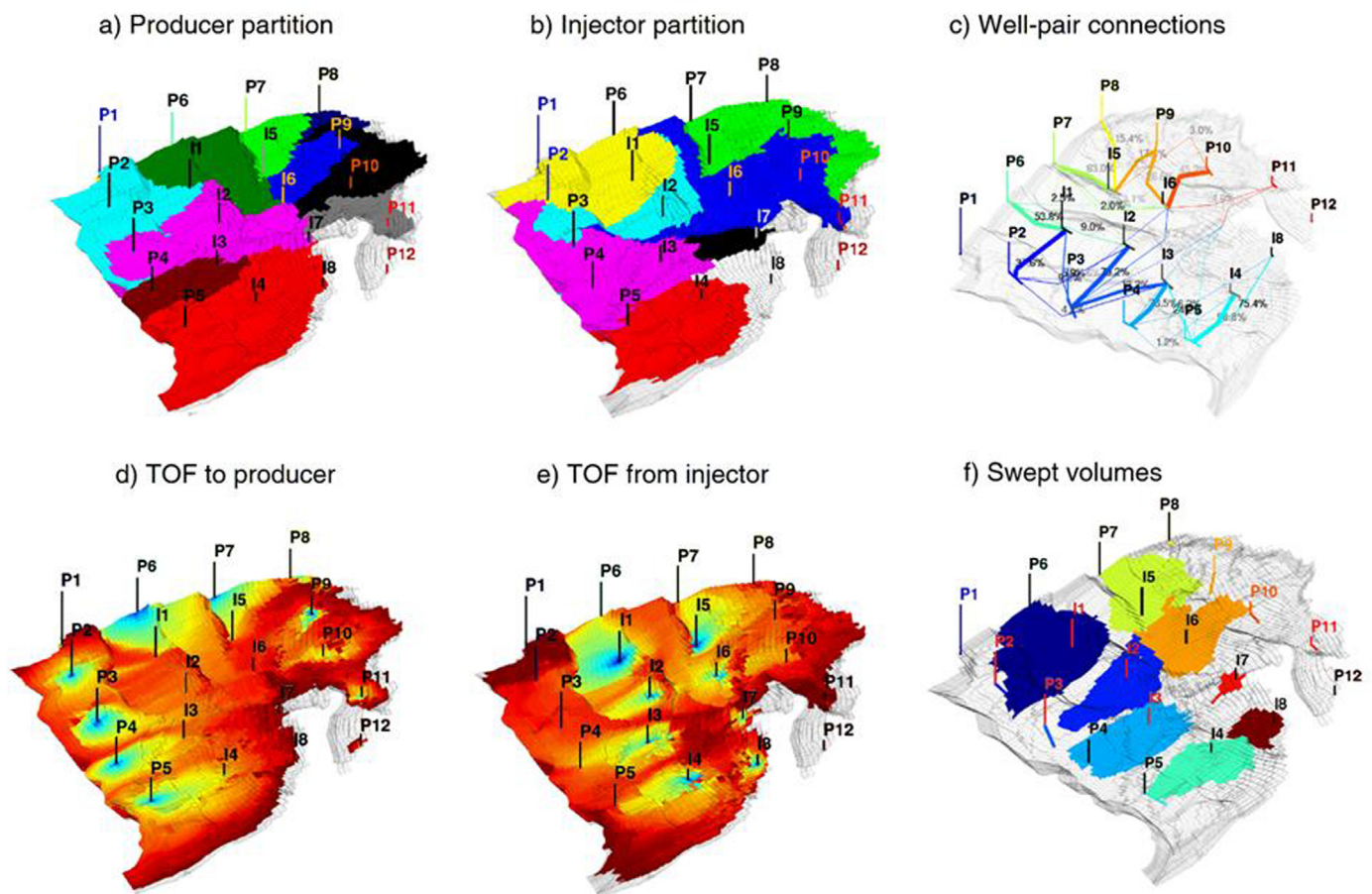

Fig. 2. a–f: Flooding visualization in streamtube compartments (top row), time of flight contours (TOFCs) and swept volumes (bottom row) for injectors and producers (after Møyner et al., 2015).

solutions to describe groundwater flow models and evolved gradually out of a school of thought propagated by Strack (1981a,b); based on earlier work by Josseling de Jong (1960). Kraemer (2003) identified that the first peer-reviewed studies applying AEM to groundwater flow problems appeared in 1981 (e.g., Strack and Haitjema, 1981a,b). The basic principles of AEM were systematically discussed in two monographs written separately by the two main advocates (Strack, 1989; Haitjema, 1995). Subsequently, AEM has been successfully applied in flow models for a wide variety of internal and external boundary conditions, physical properties and initial conditions. Models may have complex geometries, straight or curved boundaries, multiple boundaries, transient flow conditions, multiple aquifer layers, discontinuities such as leaky or impermeable faults and heterogeneities (e.g., Strack, 1999, 2003, 2006; Janković and Barnes, 1999a,b; Barnes, Janković, 1999; Anderson, 2000; Bakker, 2002, 2004; Bakker and Anderson, 2003, 2008; Bakker and Nieber, 2004; Suribhatla et al., 2004). All studies can be traced back to an initial network of Ph.Ds supervised by Otto Strack (Indiana University), some of whom subsequently raised their own groups of Ph.Ds (e.g., Henk Haitjema, David Steward, Randal Burns, Didier Graillot and Igor Janković; for detailed pedigree analysis see Kraemer, 2003, 2007). Comprehensive overviews of the body of literature based on AEM were published by Kraemer (2003, 2007) and Craig (2006). The analysis of ISI publications on ground water flow between 1980 and 2006 by Kraemer (2007) showed the relative share of the various modeling methods applied in groundwater literature: AEM (4.3%), boundary element method (6%), finite difference method (34.1%) and finite element method (55.6%). Clearly, AEM has advanced to occupy a modest share in groundwater flow modeling. Our present study aims to highlight the potential merits of applying AEM-based flow models in studies of hydrocarbon recovery optimization.

2.3. Complex potentials in AEM

A basic premise of AEM is that elementary solutions of linear differential equations may be superimposed to obtain global flow solutions that satisfy the governing equations. AEM uses bi-harmonic solutions of linear partial differential equations (including those commonly used to ensure initial conditions and boundary conditions are in place, *e.g.,* Laplace equation, the Poisson equation, the modified Helmholtz equation, and the heat equation; see Bear, 1972, ch. 7).

The principle of superposition ensures that each individual solution for a flow with bi-harmonic functions can be superposed to model composite flows. The interaction of point sources and sinks (PS), line sources and sinks (LS), impermeable lenses (IL), leaky cracks (LC) and closed boundary (CB) elements (delineated zones of higher or lower flow resistance) can be comprehensively described by the summation of the complex potentials for each flow element, provided such potentials have been validated as correct analytical solutions of the individual flow patterns:

$$\Omega(z) = \Omega_{ps}(z) + \Omega_{ls}(z) + \Omega_{il}(z) + \Omega_{lc}(z) + \Omega_{cb}(z) \tag{1}$$

The analytical elements are described by 2D polynomials giving complex potentials (and corresponding subscripts for each analytical element) that satisfy Dirichlet, Neumann, or Robin (mixed) boundary conditions (Strack, 1989). To obtain a global solution (i.e., the correct element coefficients), a system of equations is solved such that the boundary conditions are satisfied along all of the elements (using collocation, least-squares minimization, or a similar approach). The global solution provides a spatially continuous description of the dependent variable everywhere in the infinite domain, and the governing equations are satisfied.

Assuming the boundary conditions are correctly accounted for in a specific potential function and/or stream function, complex analysis (i.e., the calculus of complex valued functions; cf. Olver, 2012) links the potential function ϕ and the stream function ψ to the complex potential, Ω:

$$\Omega(z) = \phi(x, y) + i\psi(x, y) \tag{2}$$

The independent complex variable z is given by $z = x + iy$ with $i = \sqrt{-1}$. The potential function $\phi(x, y)$ and stream function $\psi(x, y)$ are respectively the real part $\Re(z)$ of $\Omega(z)$ and the imaginary part $\Im(z)$ of $\Omega(z)$. The real and imaginary solutions of $\Omega(z)$ ensure that ϕ and ψ are harmonic functions, which automatically satisfy the Cauchy–Riemann equations:

$$\partial\phi/\partial x = \partial\psi/\partial y \tag{3a}$$

$$\partial\phi/\partial y = -\partial\psi/\partial x \tag{3b}$$

The vector field is given by a complex function $V(z)$:

$$V(z) = \frac{d\Omega(z)}{dz} = \frac{\partial\phi}{\partial x} + i\frac{\partial\psi}{\partial x} = \frac{\partial\phi}{\partial x} - i\frac{\partial\phi}{\partial y} = v_x - iv_y \tag{4}$$

The velocity components (v_x, v_y) in complex space (x, iy) can be derived for any velocity field for which the complex potential $\Omega(z)$ is known. Any specific complex potential [Eq. (2)] valid for a given flow element automatically provides valid solutions of the differential equations for the line integrals described by the potential function and stream function (Strack, 1989). Although a large variety of complex potentials exists, rather than using the potential function, we focus our analysis on the stream function solution of the complex potential that can be used to visualize streamlines. However, to trace the advancement of the waterfront and time-of-flight along the streamlines we use the velocity field solutions of Eq. (4) based on the complex potential.

3. Basic assumptions

3.1. Reservoir controls with ICVs and BHAs

This study initially assumes a direct line drive constellation of wells and we run tests on the well pressures to establish the rate for each well that leads to the most effective sweep of the reservoir. First we assume homogeneous reservoir properties and then we build heterogeneities into the reservoir. Such heterogeneities or any impervious flow obstructions, as shown below, will affect the well pair connections between injectors and producers and results in sweep no longer moving uniform across the field. Response to variations in water injection rates is assumed to be monitored at the producer wells using bottomhole assemblies (BHAs; Fig. 3). Real-time hydraulic adjustments of waterflood-injection rates are assumed possible using down-hole inflow control valves (ICVs) in the injector wells. For example, Statoil installed its first hydraulically operated sliding sleeves and flow meters in injection well A-11B at the Veslefrikk field (North Sea, June 2004; Weatherford supplied the meters and WellDynamics the sliding sleeves). The injection valves are remotely controlled by the production control room. Digital decision-support systems based on subsurface and surface predictive modeling technology enable real-time data management to control the production environment. Formation pressure (and data such as temperature readings) are routinely collected from across the field and correlated against a reservoir simulation model. The down-hole injection valves are positioned and regulated to maximize field production. Operators are thus realizing significant value from establishing mechanisms for real-time data exchange between injection wells, production
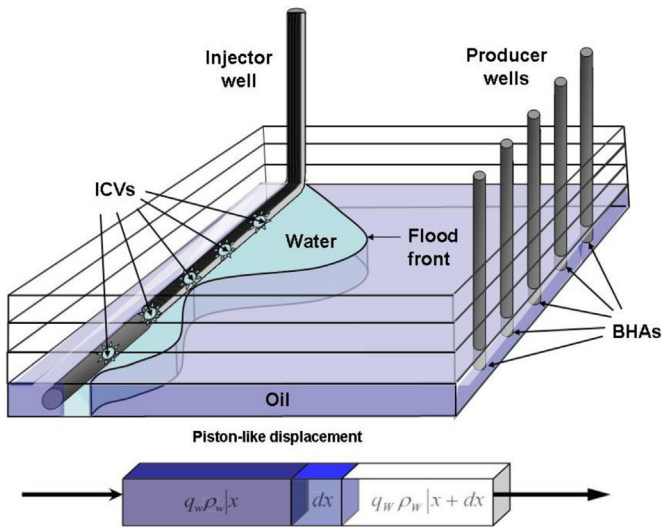
Fig. 3. Well constellation used in this study assumes one horizontal injection well with water injection rates controlled by 5 ICVs. Flooding occurs by direct line drive between the ICVs and 5 vertical producer wells where pressure can be monitored with installed BHAs.

wells and surface facilities (Unneland and Hauser, 2005).

Our models confirm that field measurement of well pressures can provide the first physical evidence of reservoir response and the information can be utilized to improve sweep efficiency by adjusting the well rates. Such a smart field optimization aims at a learning cycle which monitors and regulates the well performance based on real-time or episodic updates of the reservoir model (Fig. 4). The learning loop emulates well data with reservoir simulations akin to closed-loop modeling techniques (Zandvliet, 2008; Jansen et al., 2009). Such closed-loop systems are derived from optimal control theory originally evolved in studies of dynamic systems and applications such as in the optimization of flight paths for rockets and satellites (Bryson and Ho, 1975). The oil industry uptake of history matching of field well rates with model rates and vice versa was almost absent until the advent of smart well and smart field technologies about a decade ago (see review by Jansen, 2011). We advocate here that the learning cycle can start using synthetic data before field development begins in order to engineer possible well patterns and pressure responses such that the volumetric recovery rates of hydrocarbons will be maximized when field development decisions are made. The decision must result in the avoidance of by-passed oil to optimize the recovery factor (c.f., Smalley et al., 2009).

Well surveillance typically measures bottom-hole pressures in the producer wells using BHAs. When pressures in producer wells are unequal, the flood front pushed by a direct-line drive will, in a reservoir that is assumed homogeneous, advance at unequal
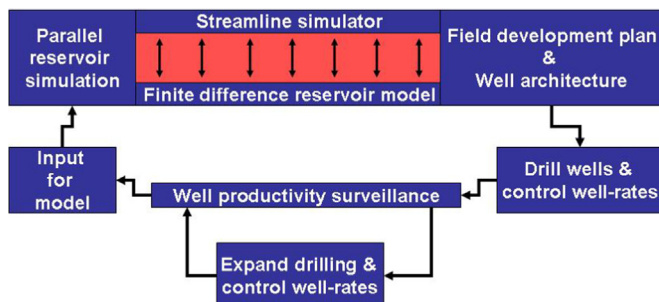

Fig. 4. Parallel reservoir simulation and field productivity optimization can reduce the delta between anticipated optimum production and actual, monitored production.

speeds (Fig. 3). To prevent early water-breakthrough, fast-flow lanes need to be delayed and slow-flow zones need to be swept faster so that the water front will reach all producer wells at the same time. The injection rates at the ICVs need to be adjusted to achieve that goal. This study is the first demonstration to show that an analytical reservoir simulator can be applied to aid field development decisions under geological uncertainty, by visualizing the impact of unknown (but probable) geological features on flow in the reservoir (validating the most likely adjustments to the a priori assumed homogeneity of the reservoir) and quantifying the impact on the timing of first water arrival in the producer wells.

3.2. Dupuit–Forchheimer approximation

A basic assumption adopted here is that the reservoir behavior can be captured in a 2D flow model confined between sub-horizontal boundaries in a well-layered reservoir (Fig. 5). The vertical and areal sweeps in the layered reservoir are determined by variations in the petrophysical properties (grain size, pore space, permeability, mineral type, e.g. clastics versus carbonates). Oil–water interaction is restricted to piston-like displacement of two immiscible and incompressible fluids with identical viscosities. Gravity and capillary effects are neglected, which is justified by a layered reservoir with flat reservoir compartments. Such compartments may occur in natural reservoirs when suites of clastics and carbonates are separated by intercalations of clay and marl, respectively. Such reservoirs are made up of relatively thin layers, which may or may not communicate via leaky interfaces. Although AEM can account for such leaky 3D communication in between reservoir sections (Strack, 1989; Haitjema, 1995) we confine our base case examples to 2D flow planes.

In our model all flow occurs within the horizontal plane of the permeable reservoir confined between a flat upper and lower impermeable boundary, corresponding to the Dupuit–Forchheimer approximation of flow so that $v_z=0$. Flow occurs only in the horizontal plane as first proposed by Dupuit (1863) and Forchheimer (1886), for groundwater flow in thin aquifers can still be useful in present-day flow simulations. To comply with Darcy flow the Reynolds number remains smaller than 1; inertia effects remain absent and only laminar flow may occur. The flow strength, m [m^2 s^{-1}] of an injector is responsible for the pressure required to overcome hydraulic resistance due to the movement of a certain flux of fluid through the reservoir space. The hydraulic conductivity, k [m s^{-1}], is the inverse of the hydraulic resistance $(1/k)$. The hydraulic conductivity of the reservoir relates to the stream function $\psi(x, y)$ by:

$$\frac{\partial \psi}{\partial y} = -v_x = k_x \frac{\partial L}{\partial x} \qquad [\text{m s}^{-1}] \tag{5a}$$

$$\frac{\partial \psi}{\partial x} = v_y = -k_y \frac{\partial L}{\partial y} \qquad [\text{m s}^{-1}] \tag{5b}$$

with Darcy velocities in the reservoir of characteristic length L. The hydraulic conductivity (k) of in a natural reservoir is dependent on the fluid properties (specific density, ρ, and dynamic viscosity, μ) and the permeability, κ [m^2], of the matrix (Bear, 1972):

$$k = \frac{\kappa \rho g}{\mu} = \lambda \rho g \qquad [\text{m s}^{-1}] \tag{6}$$

The hydraulic conductivity k for any given permeability only depends on the fluid properties; the mobility, λ, captures the most important initial state of reservoir and fluid, respectively, in the ratio of the matrix permeability [m^2] and dynamic viscosity [Pa s].
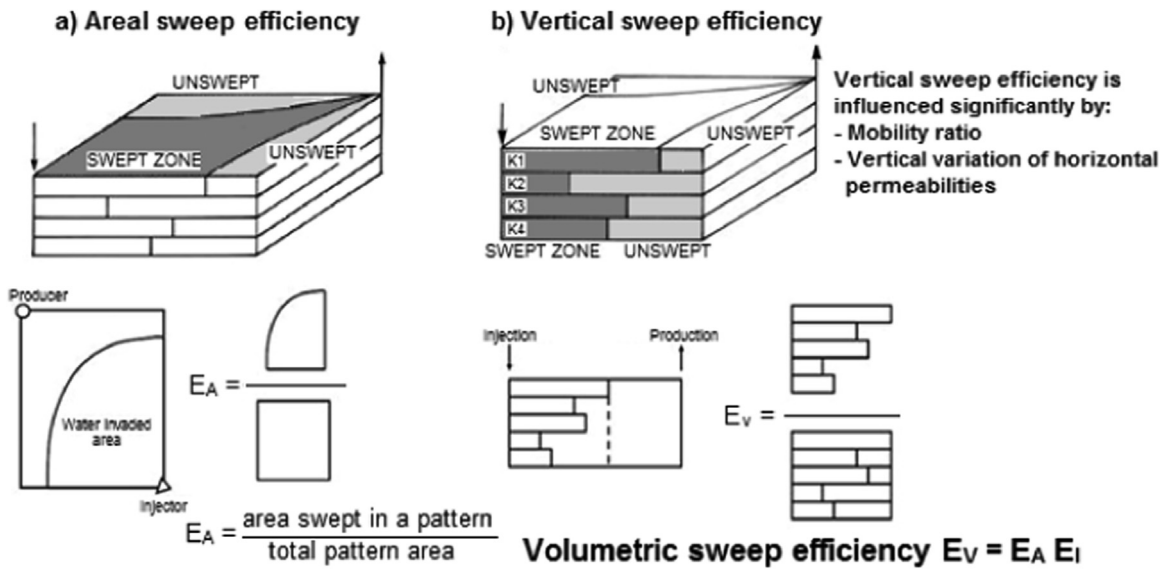
Fig. 5. Well-layered reservoir comprised of thin permeable layers separated by flat impermeable boundaries such that flow is confined to the horizontal plane. Volumetric sweep efficiency (E_v) is the product of all areal and vertical sweep efficiencies: $E_v = E_A E_I = 1/n \sum_{k=1}^{n} E_A(k) * 1/n \sum_{k=1}^{n} E_I(k)$ with n permeable reservoir layers (after Lake et al., 2014).

The waterflood is driven by the water injection with rate Q [m^3 s^{-1}], which if concentrated in a layer of thickness h can be scaled by the flow strength ($m > 0$):

$$m = Q/2\pi h \qquad [\text{m}^2\text{s}^{-1}] \tag{7}$$

We scale m by 2π because the radial velocity, u_r, of any single source would decline by $u_r = Q/2\pi rh$ and lead to a simple formula $u_r = m/r$. Because the sweep supplied by the injected water is the driving mechanism only the oil that is displaced will be produced. Likewise, a producer flux can also be described by Eq. (7) where the discharge is due to a negative well strength, i.e., $m < 0$. The specific discharge, q, is the volume of fluid moving through a unit area A of the reservoir domain per time unit:

$$Q = qA \qquad [\text{m}^3\text{s}^{-1}] \tag{8a}$$

In this study, we scale the hydraulic conductivity such that the stream function of Eq. (5a,b) can be modeled using the flow strength, m, related to the injection rate, Q, by expression (7). The specific discharge, q, is controlled by the pressure gradient and the mobility:

$$q = -\lambda\nabla(P + \rho gz) \quad [\text{m}\,\text{s}^{-1}] \tag{8b}$$

Fluid velocity, v, is related to the Darcy flux (specific discharge), q, by the porosity, n [adopting Bear's (1972) notation], which critically assumes all pore space is available for the flow (and $n > 0$ in order to exclude the extreme case where all pore space is absent for a 100% solid rock mass, i.e., $n = 0$):

$$v = \frac{q}{n} = \frac{-\lambda}{n}\nabla(P + \rho gz) \quad [\text{m}\,\text{s}^{-1}] \tag{8c}$$

Clearly, velocity adapts when the porosity, n, changes. For $n = 1$, well injection discharge, Q, meets no space constraints from any pores and flow velocity will be lower than for any other porosity value in the range $0 < n < 1$. Consequently, both the time-of-flight and fluid velocities are inversely proportional to the porosity. Jumps in the magnitude of the velocity vectors occur across porosity boundaries in the reservoir; we use expression (8c) to establish the porosity contrast across internal boundaries in our heterogeneous PASS models.

3.3. Dimensional analysis and scaling

Non-dimensional time-of-flight times for the waterfront, t^*, in PASS can be translated to real time using scaling rules for dimensional analysis (e.g., Weijermars and Schmeling, 1986). Adopting a characteristic simulation time, t_0 (for example, $t_0 = 1$ day), the dimensional time, t, is:

$$t = t^* t_0 \qquad [\text{days}] \tag{9a}$$

Of particular importance is to estimate the effective porosity, n, for the prototype reservoir correctly because a reservoir with $0 < n < 1$ will have faster time of flight than for $n = 1$ (the base case used in PASS), assuming all well rates in the model and prototype reservoirs are similarly scaled. The faster flight time occurs because for a particular injection rate the recharged fluid volume must squeeze faster forward in a lower porosity reservoir than in a higher porosity reservoir in order to accommodate the same rate of fluid injection. This follows from Darcy's law (and Eq. (8c)), which is based on experiments using sand filters (where all porosity is effective flow space). For use in porous rocks it is important to use for n the effective porosity that is available as effective flow space and not the regular pore space. Dead-end pore space with stagnant fluid should also be excluded. The dimensional time of flight of Eq. (9a) must be divided by the porosity expressed as a fraction of 1 in order to obtain the proper translation of PASS TOF to the prototype reservoir:

$$t = \frac{t^* t_0}{n} \quad [\text{days}] \tag{9b}$$

Intuitively, time of flight also is connected to the flood velocity, which becomes explicit when substituting Eq. (8c) in (9b):

$$t = \frac{t^* t_0}{q/v} \quad [\text{days}] \tag{9c}$$

Flight time scaling using Eqs. (9a) and (9b) is valid for models and prototypes that have dynamically similar boundary conditions, comparable reservoir properties, kinematic similarity of injection rates. If ether are differences in any other factors, such as the non-dimensional well rates being higher or lower than for the prototype reservoir, then the time of flight needs to be adjusted accordingly.
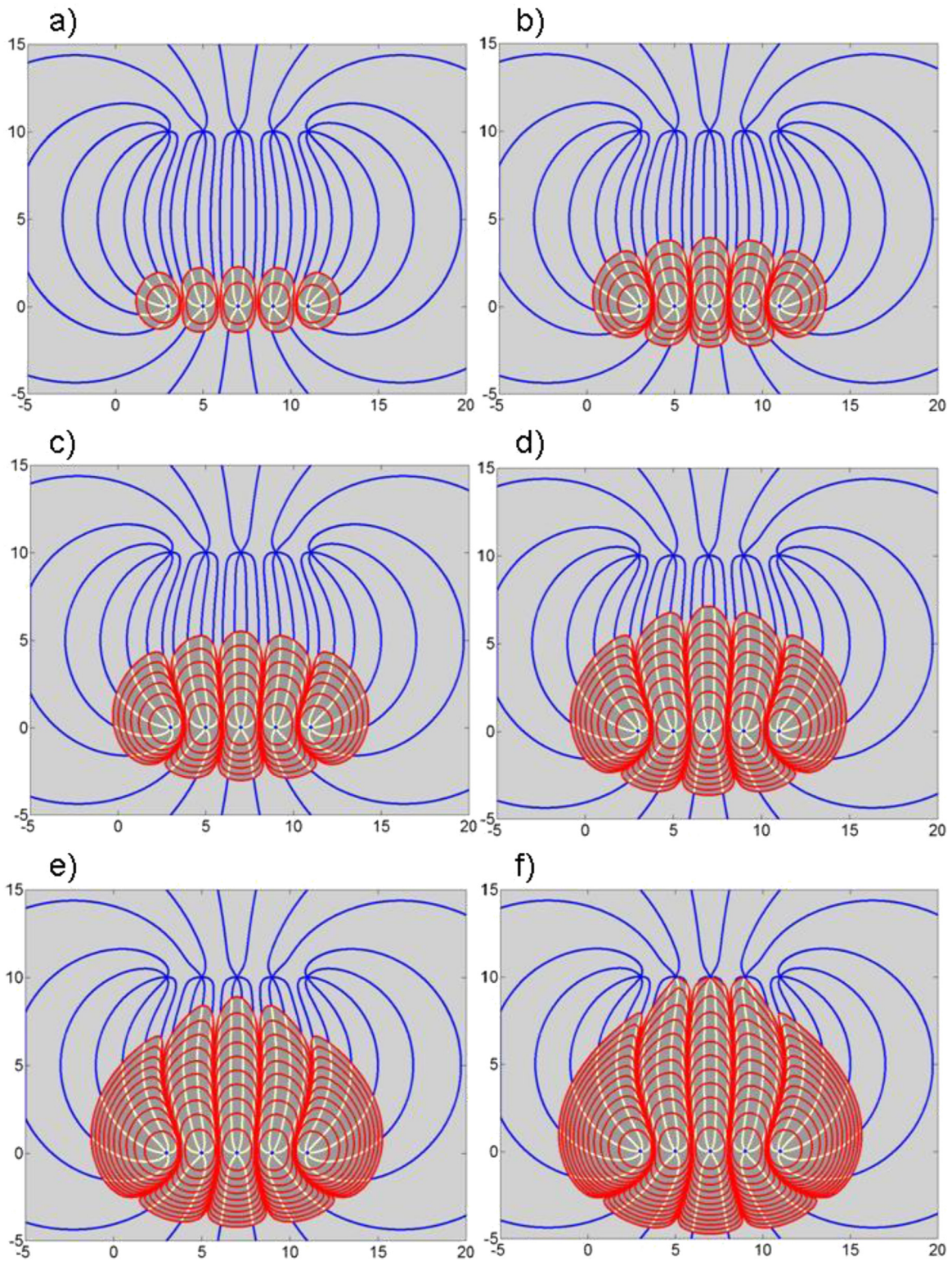
Fig. 6. Waterfront advance (dark gray body) with time-of-flight contours (TOFCs, red curves) and streamline visualization (yellow inside water body; blue curves beyond water body) using the well pattern given in Fig. 3. a–f: Time-series for homogeneous reservoir t^*=1,2,3,4,5, and 6. Time spacing between contours: 0.5. Strength sources=1; strength sinks=−1. Sources equally spaced from $3+0i$ to $11+0i$; sinks equally spaced from $3+10i$ to $11+10i$. (For interpretation of the references to color in this figure legend, the reader is referred to the web version of this article.)

Dimensional reservoir thickness, h, can be scaled using a typical unit for length, h_0 (for example, h_0=1 ft), multiplied by the non-dimensional thickness, h^*, in PASS:

$$h = h^* h_0 \quad [\text{ft}] \tag{10}$$

Positional units $(x, iy)^*$ in PASS can be translated to dimensional units using:

$$(x, iy)^* = (x/h_0, iy/h_0) \quad [\text{none}] \tag{11a}$$

So that:

$$x = x^* h_0 \quad \text{[ft]} \tag{11b}$$

$$y = y^* h_0 \quad \text{[ft]} \tag{11c}$$

The dimensional, volumetric injection rate, Q (for $Q > 0$) can be obtained from Q^* using typical time and length units, t_0 and h_0:

$$Q = \frac{Q^* h_0{}^3}{t_0} \quad \text{[ft}^3\text{day}^{-1}] \tag{12a}$$

Because the oil industry uses production and injection rate units of bbls/day rather than cubic ft per day, a scalar conversion factor is applied to expression (12a) to obtain the desired units:

$$Q = \frac{Q^* h_0{}^3}{5.6145 t_0} \quad \text{[bbls day}^{-1}] \tag{12b}$$

Our simulator uses well strength, m^*, as preferred input, which relates to volumetric flux, Q^*, as follows:

$$m^* = \frac{Q^*}{2\pi h^*} \quad \text{[none]} \tag{13}$$

Dimensional injection and production volumes, Q, can be related to non-dimensional strengths, m^*, substituting Eq. (13) in (12b):

$$Q = \frac{m^* 2\pi h^* h_0{}^3}{5.6145 t_0} \quad \text{[bbls day}^{-1}] \tag{14a}$$

and vice versa:

$$m^* = \frac{5.6145 Q t_0}{2\pi h^* h_0{}^3} \quad \text{[none]} \tag{14b}$$

PASS typically uses unit strength or multiples for m^*, run time t^*, and porosity $n=1$. Dimensional time of flight relates to model depth and injection rate by:

$$t = \frac{t^* h_0{}^3}{n Q_0} \quad \text{[days]} \tag{15}$$

Using expression (15) with dimensional values typically used in commercial reservoir simulators (*e.g.*, ECLIPSE), the one non-dimensional time unit in PASS corresponds to 0.002 days in the ECLIPSE based benchmark for time of flight based on a dimensional volumetric injection rate $Q_0 = 1000$ bbls/day for the typical prototype dimensions with unit depth $h_0 = 1$ ft, and porosity $n = 0.2$.

4. Model results

4.1. Base case models (blind injection)

The model developed here consistently uses an array of direct line drives with five injector locations (*e.g.*, ICVs in a horizontal well) and five producers (*e.g.*, vertical wells with BHAs; as in Fig. 3). The flow between the injectors and producers can be regulated by smart field technology. The flow velocity can be calculated using a complex vector field which due to point sources and sinks (injector and producer wells, respectively) is given by:

$$V(z^*) = \frac{1}{2\pi h^*} \sum_{s=1}^{n} \frac{Q_s^*}{z^* - z_s^*} = \sum_{s=1}^{n} \frac{m_s^*}{z^* - z_s^*} \quad \text{[none]} \tag{16}$$

The above assumes that for each source/sink m_s^* is scaled by $m_s^* = Q_s^*/2\pi h^*$ [Eq. (13)].

Dimensional units for $V(z)$ are [m s^{-1}] and for well strengths m_s

[m^{2}s^{-1}; using SI units]. Injector strengths are positive ($m_s > 0$) and producer strengths are negative ($m_s < 0$). The volumetric flow rate Q_s [m^{3}s^{-1}] of each well can be obtained by multiplying well strength m_s with the reservoir thickness h [m]. Fig. 6a–f shows the base case of a homogeneous reservoir with a uniform hydraulic conductivity. The progressive displacement of the waterfront is visualized by the TOFCs for non-dimensional reservoir times t^*. The basic formula for modeling source (injection wells) and sinks (producer wells) is given in Eq. (16). The time-of-flight contours (TOFCs) are tracked for water advance front and corresponding oil-withdrawal to the producer wells. The discretization time-step Δt^* can be very small and follows a first order Eulerian scheme (Zandvliet, 2008):

$$\dot{x}^*(t^*) \approx \frac{x_{k+1}^* - x_k^*}{\Delta t^*} \quad \text{[none]} \tag{17}$$

The state vector x after k time steps is given by $x_k := x(k\Delta t)$.

We compared our analytical base case with a streamline simulation using a similar well design (direct line drive, 5 injectors, 5 producers; Fig. 3) and equal injection/production strengths based on ECLIPSE (Fig. 7). The benchmark streamlines are obtained using ECLIPSE pressure data which provided inputs for Petrel after flux calculations in grid blocks based on Pollock's algorithm (Pollock, 1988; Datta-Gupta and King, 2007) built into DESTINY software developed at Texas A&M University. We conclude that the shapes of both the streamline patterns and the time of flight contours of PASS and ECLIPSE based simulations are virtually identical. Additionally, the time of flight is congruent with the scaling specified in Section 3.3. The injector ICVs in these two base case models all give equal injection rates. The TOFCs for such base case models all show that flight times for water volumes originating from the central ICVs are shorter than for the flood originating from peripheral ICVs.

4.2. Improvement of base case for homogeneous reservoir (smart injection)

For the base case of a homogeneous reservoir (Figs. 6 and 7), the TOF for water originating from I_1 and I_5 is considerably longer than for I_2, I_3 and I_4. Water from the peripheral injectors (I_1 and I_5) fans out into the left and right lateral reservoir spaces, because no further injector wells occur there. Well rates were adjusted using a simple Bernoulli pressure estimation (see Appendix A1). The well pressures in the model are monitored against the smoothness of the waterfront, which advance can be quantified and visualized by TOFCs for the water leaving the injector wells (Fig. 8a). The Bernoulli pressure is also mapped in Fig. 8b (right panel). The Bernoulli pressure in potential flow descriptions reveals the location (s) of flow stagnation points. Pressure maxima occur in stagnation points and pressure minima occur where velocities are fastest. For the base case (Fig. 8a), the pressure in the central producers (for P_2, P_3 and P_4) is slightly lower than in the peripheral producers (P_1 and P_5). These pressure differences can be minimized in a feedback loop to adjust the well-injection rates such that the TOFCs for water from all injectors equalize. Water is injected slowest at the inner injector (I_3) which therefore occupies a narrower streamtube region (Fig. 8b). For these adjusted well rates, the Bernoulli pressure field (Fig. 8b) appears to be uniform in-between the injectors and producers. The iteratively adjusted well rates are graphed in Fig. 9. Once optimum well rates were found these were used as inputs in the ECLIPSE models. Constant well rates are achieved after 2500 iterations which correspond to 0.25 non-dimension flight time in PASS. Because the benchmark software used for
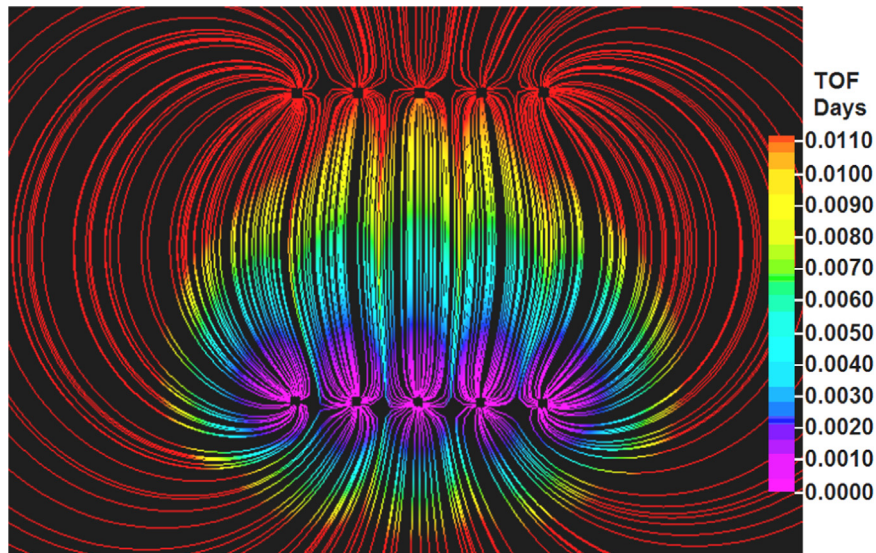
Fig. 7. Benchmark reference for PASS results of Fig. 6. Streamlines (red curves) and flood flight times (rainbow colors) are based on ECLIPSE pressure data augmented with proprietary velocity calculation based on flux balance of adjacent cell nodes. TOF for arrival of waterflood front in producer wells is 0.011 days, which corresponds to arrival time $t^*=5.5$ in the analytical model of Fig. 6e and f. (For interpretation of the references to color in this figure legend, the reader is referred to the web version of this article.)

comparison of TOFCs is based on a material balance assumption, the analytical model should also adhere to material balance. Each producer is therefore assigned the negative rate of its corresponding injector (e.g., $m^*_{P1}=-m^*_{I1}$). The TOFCs for the optimized sweep efficiency are given in Fig. 8b. The optimization algorithm is detailed in Appendix A2.

The numerical benchmark software (ECLIPSE, in unison with DESTINY and Petrel) used the analytically determined injection rates to generate streamlines and TOFCs for the optimized injection case (Fig. 8c). Comparing the streamlines in Fig. 8b (yellow/blue) with those in Fig. 8c (rainbow/red) leads to the conclusion that they are again virtually identical. Just as the streamlines, the TOFCs in Fig. 8b (red) closely match those in Fig. 8c (rainbow colors). The pressure map generated with the benchmark software is the real pressure field of the reservoir (Fig. 8c right) which differs from the Bernoulli pressure field generated based on velocity gradients (Fig. 8b, right). We prefer to use the Bernoulli pressure in the analytical model (see Appendix A1), because it shows the flow stagnation points which occur close to the wells. Knowing the location of the stagnation points is important for the optimization of the well rates, because such points should be excluded from the pressure monitoring points. Dimensional reservoir parameters used in the ECLIPSE-based benchmark are listed in Table B2 (Appendix B2).

4.3. Case A: heterogeneous reservoir (blind injection base case and smart solution)

A reservoir which, a priori, has been incorrectly thought to be homogenous will have a different flow pattern and pressure distribution than expected. We therefore investigate a hypothetical reservoir which has a heterogeneous zone in-between the injectors and producers making up the direct line drive. The heterogeneity occupies a domain located between 1/3 and 2/3 of the distance to the injector–producer pairs I_4-P_4 and I_5-P_5 (Fig. 10a).

In the analytical model the heterogeneity is modeled by four first-order line doublets (Appendix B1) which divide the heterogeneity into three equal domains (Fig. 10a). Each line doublet has unit strength per unit length and is oriented such that flow velocities are increased in the heterogeneous region, thus mimicking a higher permeability zone in each of the three domains.

The ambient reservoir permeability in the ECLIPSE benchmark

was set at 100 mD, with the high permeability zone composed of top and bottom domains of 10 times higher permeability (1000 mD), and a central band with 40 times higher permeability (4000 mD).

The streamlines generated by the analytical model (Fig. 10a) closely match those generated using the finite difference-based commercial software (Fig. 10b). In both figures, certain streamlines from injectors I_3, I_4 and I_5 are drawn towards the higher permeability zone and end up near or at producers. After a non-dimensional time of $t^*=3.5$ (Fig. 10a) some of the injected water has already traveled from injector I_4 to producer P_4 and is being produced. Producer P_5 is about to experience water breakthrough and producer P_3 will follow soon after as evidenced by the (red) TOFCs (Fig. 10a). The streamlines and TOFCs generated with the commercial software (Fig. 10b) show the same water breakthrough pattern as for the analytical simulations: breakthrough already occurred at P_4, and is about to occur at P_5, followed by P_3. The Bernoulli pressure an real pressure maps generated by respectively the analytical and the numerical codes are given in Fig. 10c and d. The Bernoulli scalar map ("pseudo"-pressure; Fig. 10c) is useful for determining the stagnation points that should be avoided as monitoring points for the flood optimization. The real pressure map (Fig. 10d) does not reveal the location of the flow stagnation points.

Again we used the Bernoulli pressure in PASS using the optimization algorithms in Appendix A2 to find the adjusted well rates that will result in equal arrival of flood in the producer wells. Fig. 11 shows the optimized sweep and the corresponding benchmark solution is also included.

### 4.4. Case B: fractured homogeneous reservoir

Another practical field situation considered is that during a geological survey an impervious fault is missed, resulting in an incorrect description of the reservoir. We therefore next incorporate such a fault in our synthetic reservoir and visualize the resulting flow and pressure distribution with both the analytical model and the commercial software for base case (equal) injection rates for all well pairs.

The impervious fault in the analytical model, visualized as a black line (Fig. 12, left colum), has its center close to the location of injector I_1, at $2+0i$. The right tip of the fault is located halfway
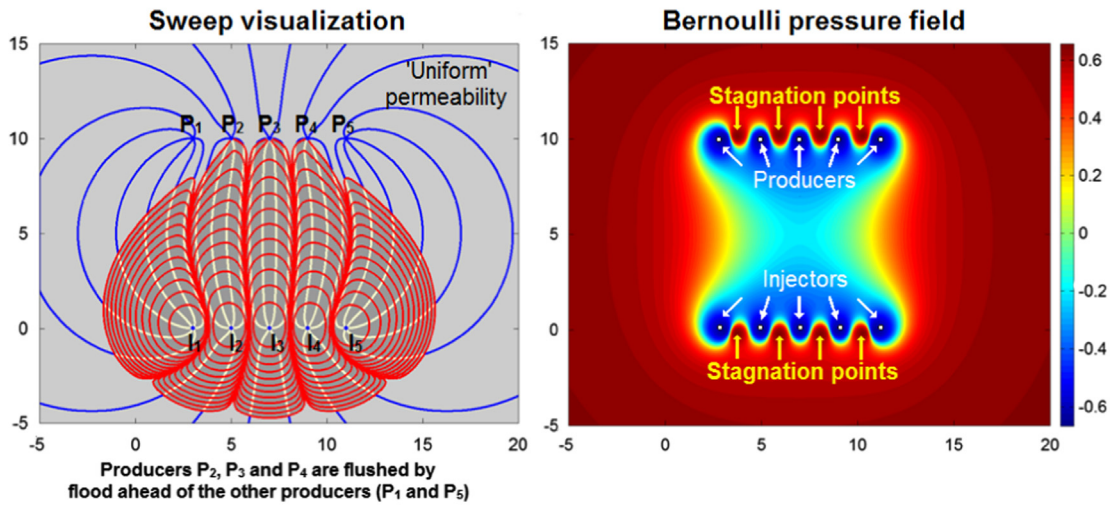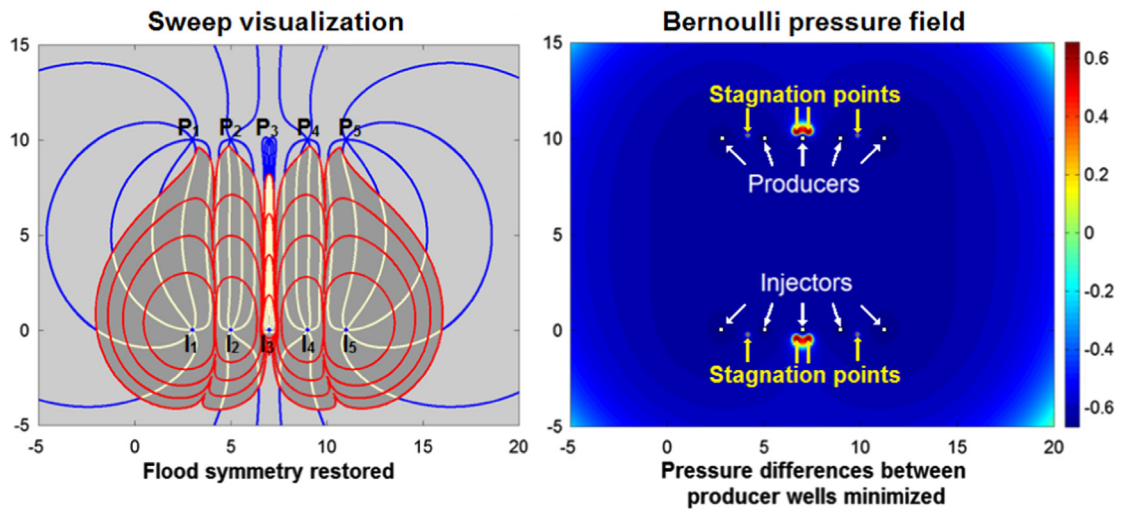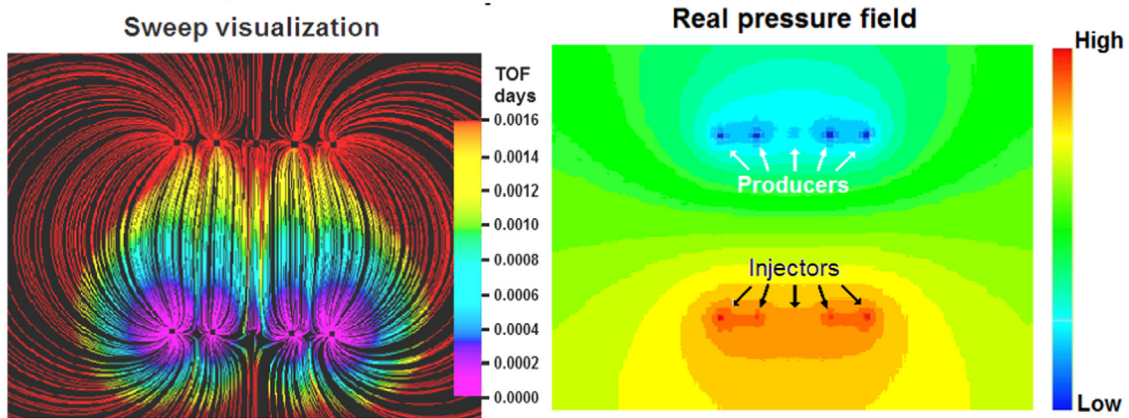
Fig. 8. a: TOFCs (left panel) and Bernoulli pressure field (right panel) in a homogeneous reservoir using equal well rates for all injectors and producers ($m^*=1$; as in Fig. 6f). Bernoulli pressure is scaled using the natural logarithm and inverse tangent. Non-dimensional time lapse between red TOFCs is 0.5. b: Optimized sweep for $t^* = 0.8$, with injector and producer strengths (from left to right) respectively [12.1; 6.5; 1; 6.5; 12.1] and [−12.1; −6.5; −1; −6.5; −12.1]. Non-dimensional time lapse between red contours: 0.2. **c**: ECLIPSE streamlines with TOFCs (left) and pressure map (right) for the optimized well rates. Scaled for a 25 ft deep reservoir, the low and high pressures are respectively 0 and 8480 psia. (For interpretation of the references to color in this figure legend, the reader is referred to the web version of this article.)
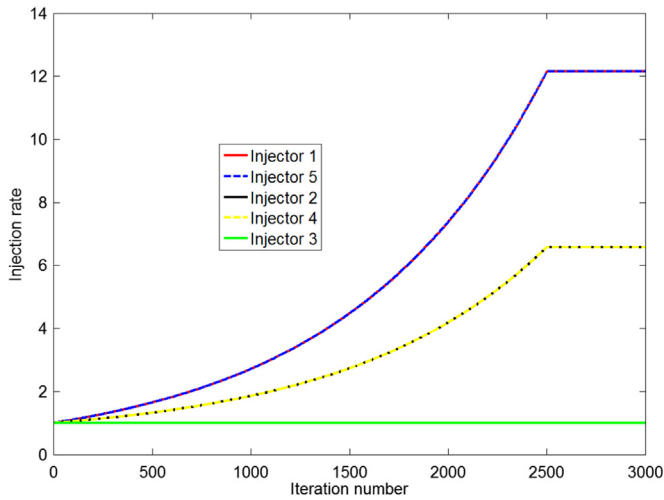
Fig. 9. Injection rates for ICVS at I_1 to I_5 iteratively adjusted by pressure monitoring of producer wells to achieve equal arrival time of flood at the producers for optimized sweep efficiency. Final well strengths are for injectors 1 and 5: $m^*=12.1$; for injectors 2 and 4: $m^* = 6.5$ and for injector 3: $m^*=1$. In order to maintain material balance, well rates for producers 1 and 5: $m^* = -12.1$; producers 2 and 4: $m^* = -6.5$ and producer 3: $m^* = -1$.

injector–producer pair I5-P5, meaning the fault is tilted at an angle of approximately 29° measure from the injector baseline and with

non-dimensional length of 20.6 (Fig. 12, left column). The analytical impervious fault is created using conformal mappings. In ECLIPSE the fault is created by specifying zero permeability for those cells that make up the fault (Fig. 12, right column).

The impervious fault as depicted in Fig. 12 has a significant influence on both the visualized streamlines and pressure distributions as it diverts the injected water strongly towards the right side of the direct line drive and it is producers. Consequentially, producer P4 (Fig. 12, top row) will experience the first water breakthrough which can be seen in the visualizations by both the analytical model and the benchmark software (Fig. 12, top row). The TOFCs of both models also are virtually identical.

The Bernoulli pressure field of the analytical model and the real pressure field calculated by ECLIPSE have little similarities (Fig. 12, bottom row). One similarity between these figures however, is that both capture the sudden change in pressure across the impervious fault. The Bernoulli pressure distribution of the analytical model shows also that the stagnation points near the injectors are shifted upward (Fig. 12, bottom left); these were originally symmetrically located in-between injectors and producers (Fig. 8a, right). The stagnation points between injectors I_1 and I_2 are shifted furthest in upward direction (Fig. 12, bottom row). The stagnation point between injectors I_4 and I_5 shows a shift towards injector I_5, instead of upwards.

Optimization of flood advance based on a feedback loop aimed at reducing the Bernoulli pressure differentials between producers
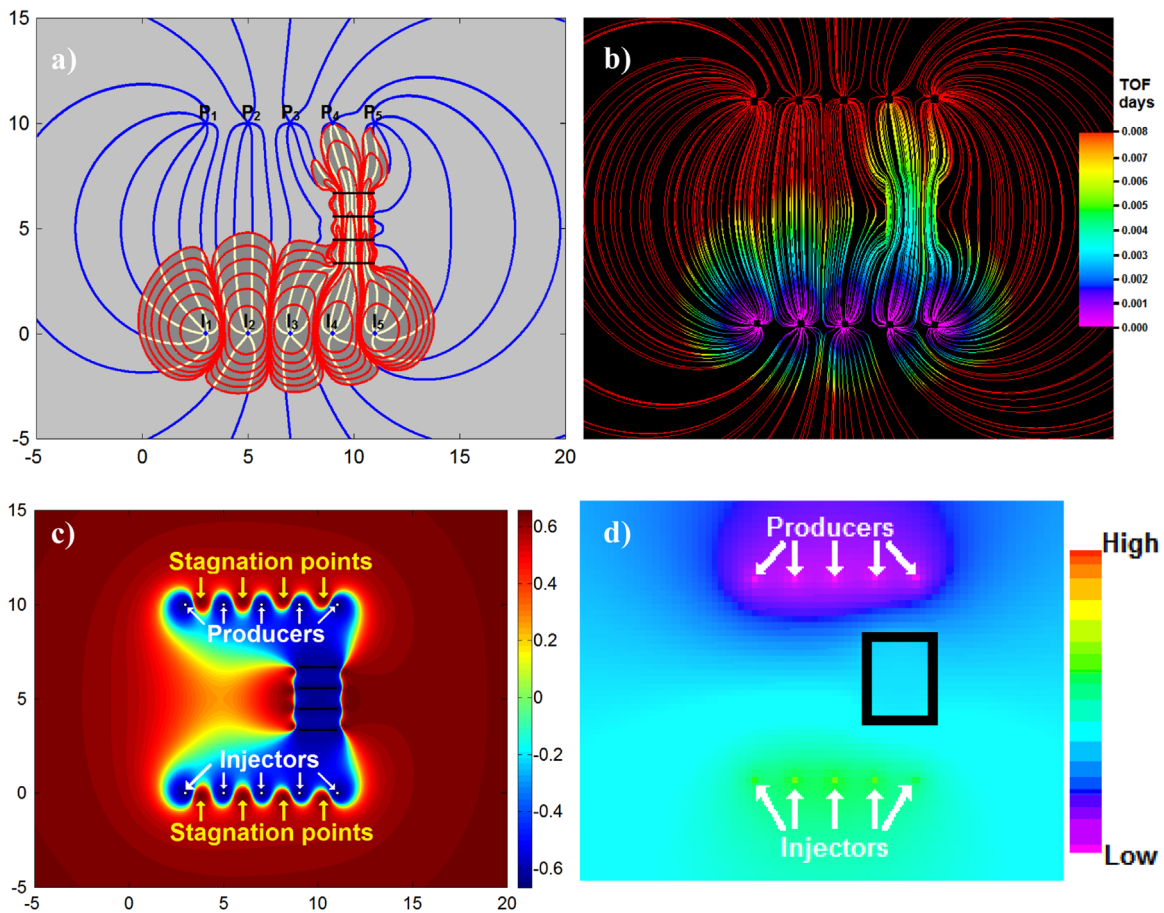

Fig. 10. a,b: Streamlines with TOFCs for equal base case well rates in a heterogeneous reservoir visualized by analytical code (a) and numerical code (b). Heterogeneity is marked in (a) by three low permeability domains separated by the four parallel horizontal lines (black). Injector and producer rates are $m^*=1$ and $m^* = -1$ respectively. Length line doublets=2; Strength line doublets=2. Non-dimensional time of flight is visualized for $t^*=3$ with 0.5 non-dimensional time lapse between TOFCs in the analytical model (a) and corresponding TOFCs in the numerical model are scaled by dimensional color fringes (b). c: Bernoulli pressure map. d: Real pressure map; location of high permeability zone (1000 mD as compared to ambient 100 mD) is outlined by black rectangle. (For interpretation of the references to color in this figure legend, the reader is referred to the web version of this article.)
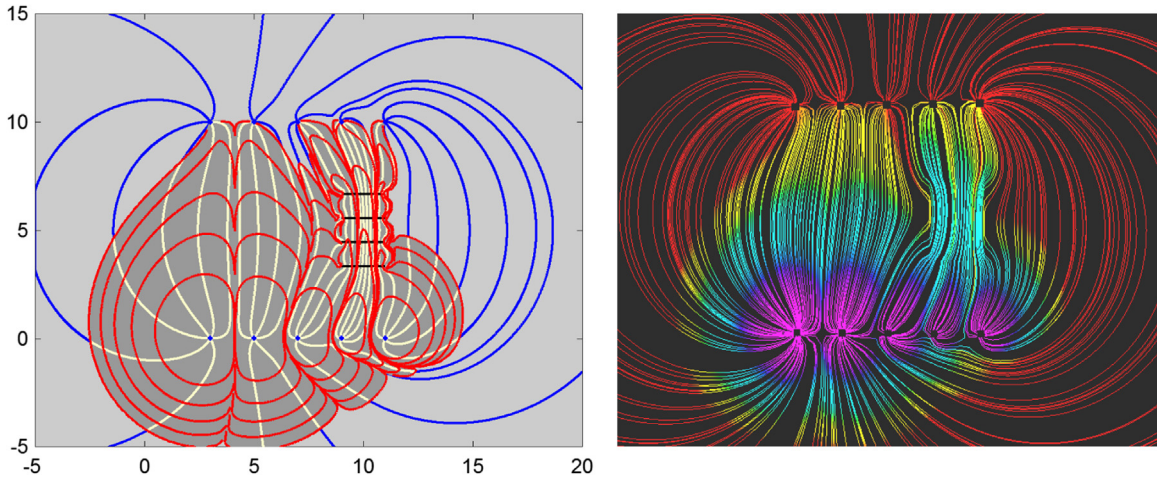
Fig. 11. Improved flood sweep due to adjustment of well rates. Analytical streamlines and TOFCs (left) and numerical solutions (right) match closely. The optimized case used injector strengths: I1=4.818, I2=3.14, I3=1.911, I4=1 and I5=1.5295; Producer strengths: P1=−4.818, P2=−3.14, P3=−1.911, P4=-1 and P5=−1.5295. Runtime 2.5 and non-dimensional time between contours is 0.5.

(Appendix A2) was inconclusive. To achieve equal arrival times at all producers for Case B would most probably require very high production values in producer P_1 and relatively much lower values for the other producers. As the pressure in the producers in this setup will be quite different from each other, the pressure distribution might be useful in determining better wellbore locations such as parallel to the fault direction.

5. Discussion

5.1. Generic observations

This study assumes a certain well design (direct line drive, 5 injectors, 5 producers; Fig. 3) and improves waterflooding efficiency by controlling the pressure gradient near production wells by continual adjustments of water rates at the injection wells. During the production phase of an operating field, the measured injection rates and pressures in the producer wells provide input
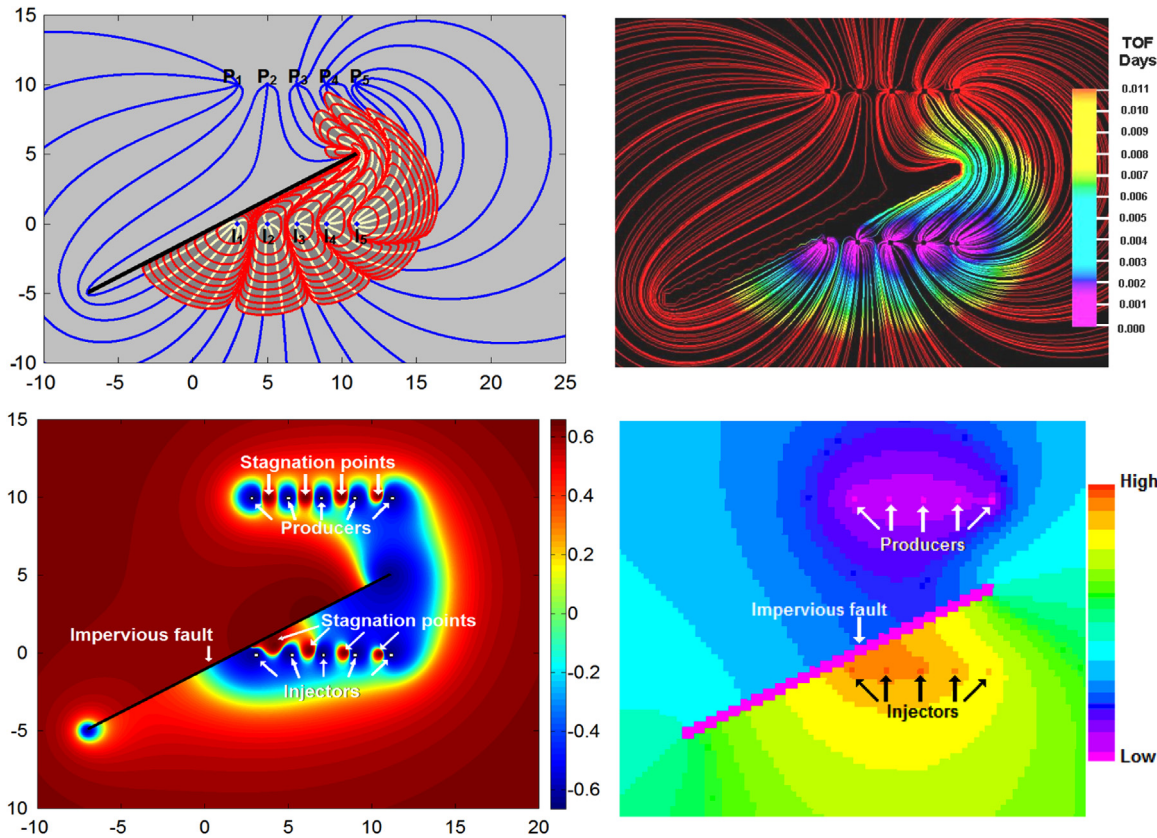

Fig. 12. Top row: Streamlines and TOFCs for waterflood advance in a homogeneous reservoir with an impervious fault. Analytical solution (left) is closely matched by numerical solution (right). Fault center is at $2+0i$, angle 29° and length $l \approx 20.6$. Right tip located halfway injector–producer pair I_5-P_5. Total non-dimensional time in analytical model (left) $t^*=5$; time between contours 0.5. Bottom row: Bernoulli pressure for analytical model (left) was scaled using natural logarithm and inverse tangent. Real pressure (highs and lows) from ECLIPSE based model (right) scaled for a 10 ft deep reservoir ranges between 0 and 10,000 psia.

data to refine the simulation of waterflooding as demonstrated in numerous previous studies (e.g., Asheim, 1987, 1988; Sudaryanto and Yortsos, 2001; Brouwer and Jansen, 2004; Fyrozjaee and Yortsos, 2006; Jansen et al., 2009). History matching with the monitored well rates can improve the accuracy of the model prediction of the time of flight of the water front. Real-time adjustments can be made to the well rate settings (ICVs) in the field based upon the improved model results in an iterative process until satisfactory convergence is achieved between the measured and simulated production data. The alternative solution of so-called bang-bang control using cheaper on–off injection valves rather than scalable ICVs was not considered here. The optimized injection rates deduced here could be implemented with bang-bang valves instead of more costly ICVs provided the former are capable of high frequency on–off oscillations, but such functionality may not be practically feasible based on current user specifications and design for such valves. Consequentially, we assume ICVs are afforded partly based on their crucial contribution to NPV optimization.

Previous studies of front controllability in two-phase porous media have suggested that the presence of geological heterogeneities, such as high-permeability streaks are an essential prerequisite for influencing significantly subsurface flow through the manipulation of well rates (Fyrozjaee and Yortsos, 2011; Jansen et al., 2009; Jansen, 2011). We agree with previous authors that such heterogeneities may cause larger distortions of the flood front and provide stronger signals for adjusting the well rates to reduce the distortions. Our comparison of the flood advance in the homogeneous and heterogeneous model reservoirs shows that a finite well array in direct line drive forces the flood front to move fastest in either the central zone or a high permeability streak between the injector and producer wells. Our results indicate that field development with finite well arrays introduces differential flood advancement and variations in TOF when the rates of all injectors are kept identical. For the water front to arrive simultaneous in the producer wells, the injection rates of ICVs need to be adjusted real-time to compensate for the peripheral spreading of the injected water from ICVs at either end of the horizontal injection well.

5.2. Our results

Our control algorithms used a feedback loop that acts when pressure differentials develop near the producer wells. The producers are given an initial rate in the model. The pressure field around each well is a function of the velocity, which in potential flow is a direct relationship with the velocity vector. The injection rate of the ICVs is adjusted in a feedback loop such that the differences in pressure around the producers are minimized. In this way, the appropriate injection rates are established for the ICVs. The objective is to optimize the displacement efficiency of the water front. This means avoidance of premature water breakthrough as controlled by pressure differentials near the producer wells. In a real field, the pressure in the wells is given by the BHAs (Chorneyko, 2006) and injection rates can be adjusted using the sliding sleeves of the ICVs.

Our synthetic flood models include two distinct examples where the properties of the reservoir, which were assumed previously unrecognized/unknown at the time the field was developed with the direct line drive well layout, leads to premature water breakthrough in wells P3 and P4. Case A of premature water arrival is due to a heterogeneous high permeability zone (Fig. 10) and Case B resulted from a hidden impervious fault zone (Fig. 12). In contrast, the a priori assumed reservoir model with homogeneous reservoir properties, for which we optimized the well rates (Fig. 8b and c) cannot result in premature water

breakthrough in any peripheral well pair. The observation of premature water breakthrough in any peripheral wells would indicate that the reservoir model was based on incomplete subsurface information. Even long before such premature water breakthrough occurs, history matching of the well pressures can be used to check how the original physical model of the reservoir can be adapted to better predict the field's future performance. Our model can determine whether Case A or B is the more plausible explanation of any observed deviation of well pressure responses to well rate adjustments (at the installed pumps) based on the originally intended flood optimization using the homogenous reservoir base case model as a starting point.

The procedure to test which of the two options (Case A or B) could be responsible for a future occurrence of premature water breakthrough is as follows. For Case A the pressures in the production wells (Fig. 12 bottom row) will differ (due to the impact of the high permeability zone on the flow field) from those due to the well rates for the optimized homogeneous base case (Fig. 8b and c). If such pressure deviations are monitored and noted early in field life, the optimization algorithm of Appendix A2 can be used to adjust well rates for Case A reservoir conditions in an attempt to restore the well pressures and ensure more synchronized water arrival as shown in Fig. 11. If Case A is indeed responsible for the observed pressure distribution among the wells, the well adjustment intervention should be successful. Adjustment of the well rates should result in a reduction of the deviating pressure differentials between the wells. In contrast, if Case B is responsible for the departure from homogenous reservoir behavior (Fig. 12), the adjustment of any well rates cannot result in equalized water flood arrival times due to the presence of the fault and pressures cannot be manipulated as much as in Case A (Figs. 10 and 11). History matching of the well rates and continuous monitoring of the well pressures in the early stages of the flood program can thus constrain the anticipated flood arrival times. Based on the demonstrated synthetic cases of possible subsurface scenarios, we argue that the analytical streamline simulator can be used as a practical tool to test the likely causes (Case A or B, or any other scenarios not tested here) that may explain deviations from the anticipated reservoir response to a flood program, particularly when subsurface data are scarce.

We optimized the sweep using model pressures in the producer well to adjust the injection rate in our synthetic cases. A reservoir model based on real data may likewise require different injection rates to synchronize the arrival time of floodwater in the producer wells. For example, the Brugge set of field data can be used for 3D reservoir optimizations using many different state-of-the-art reservoir simulators (Peters et al., 2010, 2013). Such simulators are designed to handle complexity which is useful when larger sets of field data become available during the field operations and adjustments are made real-time as operations gather more data. Our analytical streamline simulator (PASS) provides a complimentary tool that can be used for very quick runs to test the performance of proposed field development scenarios. The present study advances the applications of PASS to include smart field solutions.

5.3. Comparison of PASS computation times with numerical benchmark

Computation time of a single streamline in the analytical model depends mainly on the chosen time step size Δt^* and total simulation time. Obtaining smooth TOFCs requires tracing closely spaced particle paths which leads to increased computation time. In each of the PASS sweep visualizations presented in this paper we use 361 streamlines per injector, making up a total of 1805 streamlines. Additionally, to obtain smooth streamlines each

simulation used time step size $\Delta t^* = 0.0001$. Using such a time step size means that as total simulation time of 5 requires 50,000 time steps. The computation time required using 1805 streamlines and 50,000 time steps is about 2 min. Finally, visualization of the streamlines takes less then half a minute.

For the numerical simulator there are three main steps which take computation time. First, we run ECLIPSE to obtain the pressure and flux data for each cell for which computation time will depend on the grid dimensions used. For the ECLIPSE model we have 50,000 cells which take about 1.5 min to solve. Next, we run DESTINY software using the model data from ECLIPSE output file and transfer to the internal data format of DESTINY which performs the streamline tracing data. The time for this step depends on the number of streamlines (in the figures we have 280 streamlines) and the grid dimensions ($250 \times 200 \times 1$ in this case). This process step takes about 3 min computation time. In a final step we load all results in Petrel to visualize the streamline trajectories and the TOF values, which will take another half minute.

The computation time and number of data transfers in PASS are shorter and fewer than in the numerical streamline tracing method. Both methods have their merits. However, the closed-loop well rate optimization enabled by PASS is less simply implemented in the numerical streamline tracing method, because of the data transfers between three software packages. By comparing the flow rates and well pressures in the model field with those monitored in the actual reservoir, reactive waterflood control can be supported by PASS. Another major advantage over numerical modeling with spatial discretization (physical discretization) of reservoir parameters is that continuous solutions are obtained, and numerical diffusion is absent.

6. Conclusions

Streamline visualization in flow simulations based on closed-form analytical solutions can provide computationally efficient, fast reservoir proxies to quickly identify a number of key aspects relevant for improving waterflood management. This approach provides systematic insight in the flow behavior of reservoirs in response to various well deployment and production scenarios. In the design phase, waterflood front flight-paths can help to find the well architecture for injectors and producers that creates the most efficient sweep. Visualizations of well-pair connections (of communicating injectors and producers) will avoid the realization of well constellations where less efficient wells would suppress the recovery speed. Armed with this information it is possible to develop a responsive reservoir management strategy. The optimized well design obtained with fast streamline visualizations during field development planning can be incorporated in advanced FD reservoir models when more geological and reservoir performance data are built into the reservoir model for further flood optimization as reservoir characterization matures.

Appendix A. Pressure and optimization algorithms

A1. Fluid pressure in potential flow

In reservoir simulations using viscous flow descriptions, the pressure commonly drops in the downstream flow direction. Pressure near the injector wells is then slightly higher than in the producer wells (Fig. A1). In our potential flow description such regional pressure gradients are neglected when frictionless flow is assumed. The principal pressure behavior in potential flow is illustrated here for flow around a frictionless cylindrical inclusion of radius a and uniform far-field flow velocity U_∞. The corresponding stream function ψ and potential function ϕ using cylindrical coordinates (r, θ), are:

$$\Psi(r, \theta) = U_\infty[r - (a^2/r^2)]\sin\theta \tag{A1-a}$$

$$\phi(r, \theta) = U_\infty[r + (a^2/r^2)]\cos\theta, \tag{A1-b}$$

The streamlines are map in Fig. A2 a. Flow components v_r and v_θ can be derived from either the stream function or potential function as follows:

$$v_r = \delta\phi \, / \delta r = (1/r)(\delta\Psi/\delta r) \tag{A2-a}$$

$$v_\theta = -\delta\Psi/\delta r = (1/r)(\delta \, /\delta r). \tag{A2-b}$$

Applying the differentiation of Eq. (A2a and b) to Eq. (A1a and b) yields radial and tangential velocity components for the potential flow:

$$v_r = U_\infty[1 - (a^2/r^2)]\cos\theta \tag{A3-a}$$

$$v_\theta = -U_\infty[1 + (a^2/r^2)]\sin\theta \tag{A3-b}$$

The pressure induced by the potential flow on the inclusion is given by (e.g., White, 2011).

$$P = (1/2)(\rho U_\infty^2)(2\cos2\theta - 1) \tag{A4}$$

Pressure maxima occur for $\theta = 0$ and $\theta = \pi$ and pressure minima for $\theta = (\frac{1}{2})\pi$ and $\theta = (3/4)\pi$:

$$P_{MAX} = (1/2)\rho U_\infty^2 \tag{A5-a}$$

$$P_{MIN} = -(1/2)\rho U_\infty^2 \tag{A5-b}$$

The full pressure field around the inclusion as a function of location (r, θ) is:

$$P = (1/2)(\rho U_\infty^2)[2(a^2/r^2)\cos2\theta - (a^4/r^4)] + P_\infty \tag{A6}$$

The far-field pressure P_∞ occurs far from the wellbore. It is easy to see from Eq. (A6) that for $r \to \infty$ the pressure $P = P_\infty$. Everywhere in the potential flow pressures for $\theta = 0$ and $\theta = \pi$ are identical, which is known as d'Alembert's paradox. Although the model shows no pressure gradient in the downstream direction,
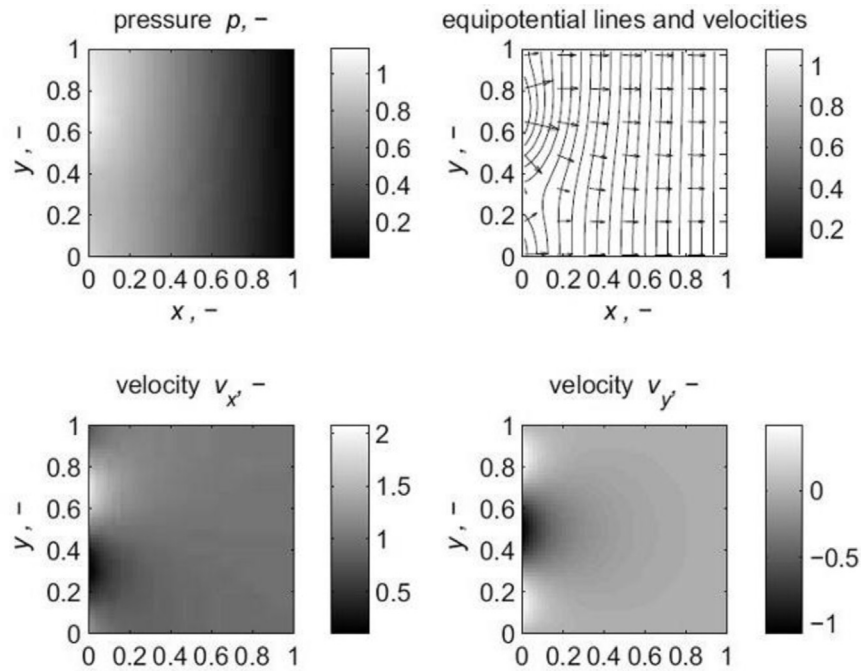
Fig. A1. Parallel reservoir simulation and field productivity optimization can reduce the delta between anticipated optimum production and actual, monitored production. For details of such models see Jansen et al., 2009, from which we reproduced above model principles.

we can still map pressure differences based upon the spatial velocity changes (Fig. A2 b). The same principle is used in our pressure field simulations in the main text.

Alternatively, pressure can be derived using the real part of the complex potential $\Omega(z)$ constituted by the potential function $\phi(x, y)$, which gives the real pressure across the flow field $P(x,y)$ as follows (Datta-Gupta and King, 2007):

$$\phi(x, y) = -\lambda P(x, y) \quad [\text{Pas}] \tag{A7}$$

Translation of the pressure by the real part of the complex potential used in PASS can be scaled for actual reservoir pressures, but this requires scaling with effective porosity similar to the explanation of dimensional flight times [see Eq. (9b)]. Reservoir pressure for the same fluid flux will be higher by a fractional amount equal to the inverse of the effective porosity. For example, for PASS $n=1$ and prototype $n=0.2$, PASS pressures will need to be dimensionalized plus multiplied by a factor 5 to obtain the reservoir pressures.

A2: Optimization algorithm

The feed-back loop algorithm used for Fig. 9 is as follows:
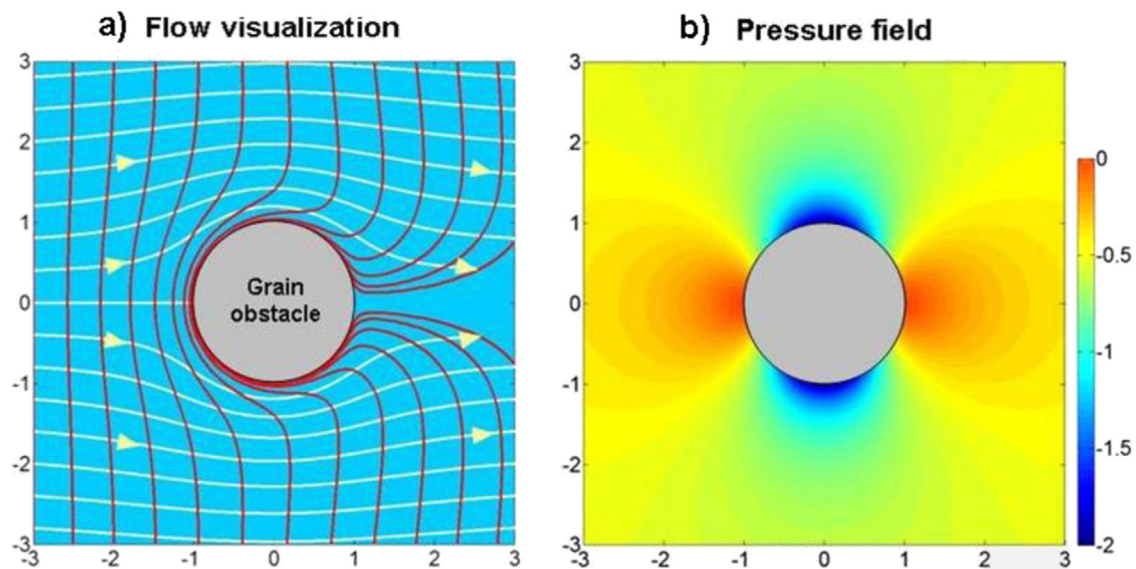1. Set initial strengths of all injectors to 1 and producers to −1:

Fig. A2. a: Stream line pattern for non-inertial flow. b: Pressure highs (red) and lows (blue) calculated using Bernoulli's pressure function [Eq. (A6)]. (For interpretation of the references to color in this figure legend, the reader is referred to the web version of this article.)

$$m^*_{inj}(0) = 1(\text{for} - \text{all} - \text{injectors}); \quad m^*_{pro}(0) = -1(\text{for} - \text{all} - \text{injectors})$$

2. Calculate Bernoulli pressures directly below producers and find the maximum pressure difference:

$$diff(0) = \max_{pro} P_{pro} - \min_{pro} P_{pro} \tag{A8}$$

3. Set the next time step: $t_{k+1} = t_k + \Delta t$
4. For the next time step, do the following:
a. Keep the injection rate of the middle injector equal

$$m_{middleinjector}(t_{k+1}) = m_{middleinjector}(t_k) \tag{A9a}$$

b. Multiply the injection rate of the outer two injectors with a constant larger than but close to 1

$$m_{outerinjector}(t_{k+1}) = m_{outerinjector}(t_k) \cdot c \tag{A9b}$$

c. Let all other injectors have a rate equal to the mean of the injection rate of the two neighboring injectors of the previous time step:

$$m_{innerinjectors}(t_{k+1}) = \frac{m_{injectorleft}(t_k) + m_{injectorright}(t_k)}{2} \tag{A9c}$$

5. Calculate Bernoulli pressures directly at the producers and find the maximum pressure difference:

$$diff(t_{k+1}) = \max_{pro} P_{pro} - \min_{pro} P_{pro} \tag{A10}$$

6. If the maximum pressure difference of the next time step is not lower than the maximum pressure difference of the previous time step, then the changes in injection rates are rejected:

$$\text{if } diff(t_{k+1}) \geq diff(t_k), \text{ then } m_{inj}(t_{k+1}) = m_{inj}(t_k) \tag{A11}$$

7. Repeat steps 3 to 5 for every time step. The adjusted injection rates for I_1 to I_5 are graphed in Fig. 9.

For Case A, instead of adjusting injector rates as in Eqs. (A9a–c), the algorithm is based on the ratios of the Bernoulli pressures relative to the producer with the highest pressure:

$$m_{injectorj}(t_{k+1}) = m_{injectorj}(t_k) \cdot \frac{\max P_{pro}}{P_{proj}} \tag{A12}$$

Appendix B. Model tool details PASS and ECLIPSE-based benchmark

B1: Closed boundary elements (PASS)

Cauchy integrals were applied by Muskhelishvili (1953, 1958) to model regions of distinct elastic behavior. Goodier (1936) has shown that the descriptions for incompressible elastic deformation and viscous flow are mathematically identical and can be transmutated by switching the shear modulus with the kinematic viscosity and the strain with the strain rate (Schmid and Podladchikov, 2003). Strack (1989) adopted the approach of Muskhelishvili (1958) and defined two complex potential as Cauchy integrals for the internal and external domains of a closed boundary element (Fig. B1):

$$\Omega^+(z) = -\frac{1}{2\pi i} \oint_C \frac{\Omega^+(\delta)}{z - \delta} d\delta \quad (z \text{ in } D^+) \tag{B1a}$$

$$\Omega^-(z) = +\frac{1}{2\pi i} \oint_C \frac{\Omega^-(\delta)}{z - \delta} d\delta \quad (z \text{ in } D^-) \tag{B1b}$$

The two Cauchy integrals may be combined into a potential function for the entire space (Strack, 1989):
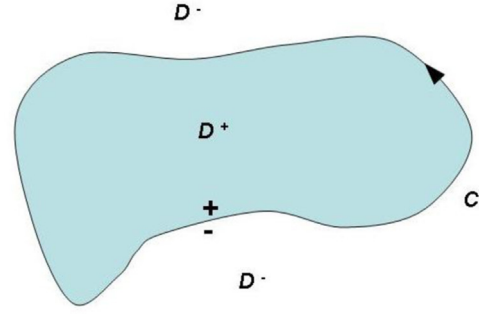

Fig. B1. Closed boundary element of increased hydraulic resistance described by Cauchy integrals.

$$\Omega(z) = \Omega^+(z) + \Omega^-(z) = -\frac{1}{2\pi i} \oint_C \frac{\Omega^-(\delta) + \Omega^+(\delta)}{z - \delta} d\delta \tag{B2}$$

According to Strack (1989) fluid flow across heterogeneities that have different flow resistance can be modeled by stringing together line doublets into closed boundary elements. Boundary elements made up of collated line doublets outline an internal zone with flow resistance different from the external domain. The stream function should remain continuous across such boundaries but the abrupt flow rate changes render the equipotential discontinuous (jumps occur) across such boundaries (Strack, 1989). Dirichlet boundary conditions apply initially: the far-field flow is uniform and rectilinear and elements affecting the hydraulic conductivity only occur in the near-field.

Several strength distributions are possible along the line doublet representing the boundary of a zone with a particular hydraulic conductivity. "First-order" line doublets have a strength distribution such that the strength is uniform in each location along their boundary interval (Fig. B2a). When first-order line doublets are used to outline an inhomogeneity, this does not always yield accurate results because equipotentials vary along the boundary and singularities develop at the tip of line doublets. The singular behavior can be avoided by giving line doublets a strength that varies along their length (Fig. B2b). These so-called "second-order" line doublets can account for a steep discontinuity in hydraulic conductivity with a higher accuracy than first-order line doublets, because the lateral variations in the equipotentials can be suppressed (Strack, 1989).

In our study we limit our attention to a first-order approximation of domains with anomalous hydraulic conductivity. First order line doublets were arranged such as to create heterogeneous reservoir zones of either lower or higher hydraulic resistance which affects the sweep efficiency (Fig. B3). Comparing the two sweep patterns generated, the TOFCs for the high permeability zone (marked with two black lines) causes the waterfront to arrive at the producers (Fig. B3, top left) much earlier than in the case of the low permeability heterogeneous domain (Fig. B3, top right). The Bernoulli pressure field for the high permeability zone (Fig. B3, bottom row) visualizes low pressures (blue) where water can flow easily and high pressures (red) has a higher resistance to fluid flow due to the lower permeability The Bernoulli pressure field for the low permeability zone (Fig. B3, bottom right) visualizes how fluid flow avoids the central domain. Due to the low permeability there is more resistance to flow and this is visualized by the lack of low pressure values in the central domain: instead of blue the dominating color is red with yellow fringes (Fig. B3, bottom right).

ECLIPSE-based streamlines (Fig B4) provide close matches with the analytical streamline patterns (Fig. B3). For the high permeability zone case (Figs. B3 and B4, top left), we see that the streamlines curve inwards because of the high permeability. The floodfront arrives at all five producers nearly at the same time. But
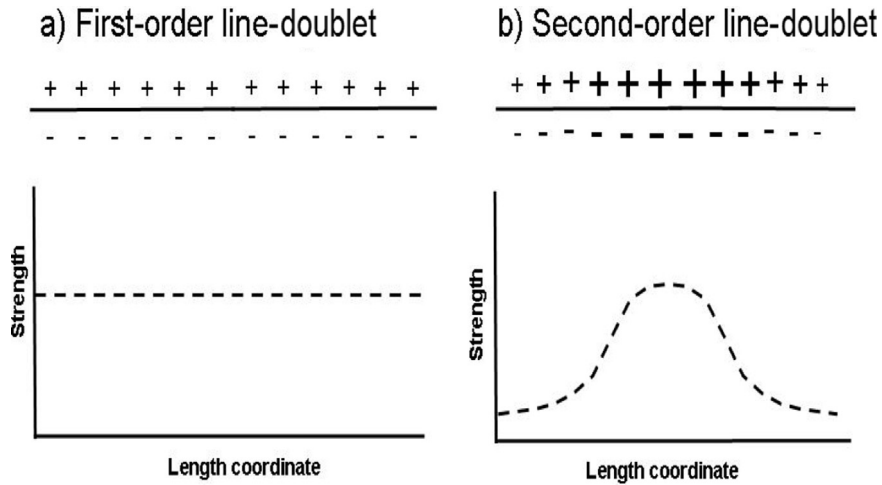
Fig. B2. Strength distribution along first-order line-doublet is constant (a), and variable for second-order line-doublet (b).

for the low permeability case (Figs. B3 and B4, top right), the fluid flows outwards because of the low permeability domain that diverts the flow between the injectors and producers. The flood front arrives first at producers 1 and 5. The pressure in the injectors for the high permeability zone (Fig. B4, bottom right) is lower than for injectors near a low permeability zone (Fig. B4, bottom left) for otherwsie equal well rates. The occurrence of anomalously high pressures in the injector wells provides a strong diagnostic indicator for the presence of a depressed hydraulic conductivity between the injectors and producers. Reversely,

unexpected low pressures in the injector wells suggest the presence of anomalously high permeability zones.

The permeability contrast of the two adjacent zones with permeabilities κ_1 and κ_2 can be inferred from the acute angles α_1 and α_2 between the boundary and the streamline tangent at either side of the boundary between the respective permeability domains, which is known as the Law of refraction of streamlines (Irmay, 1964; Bear, 1972):

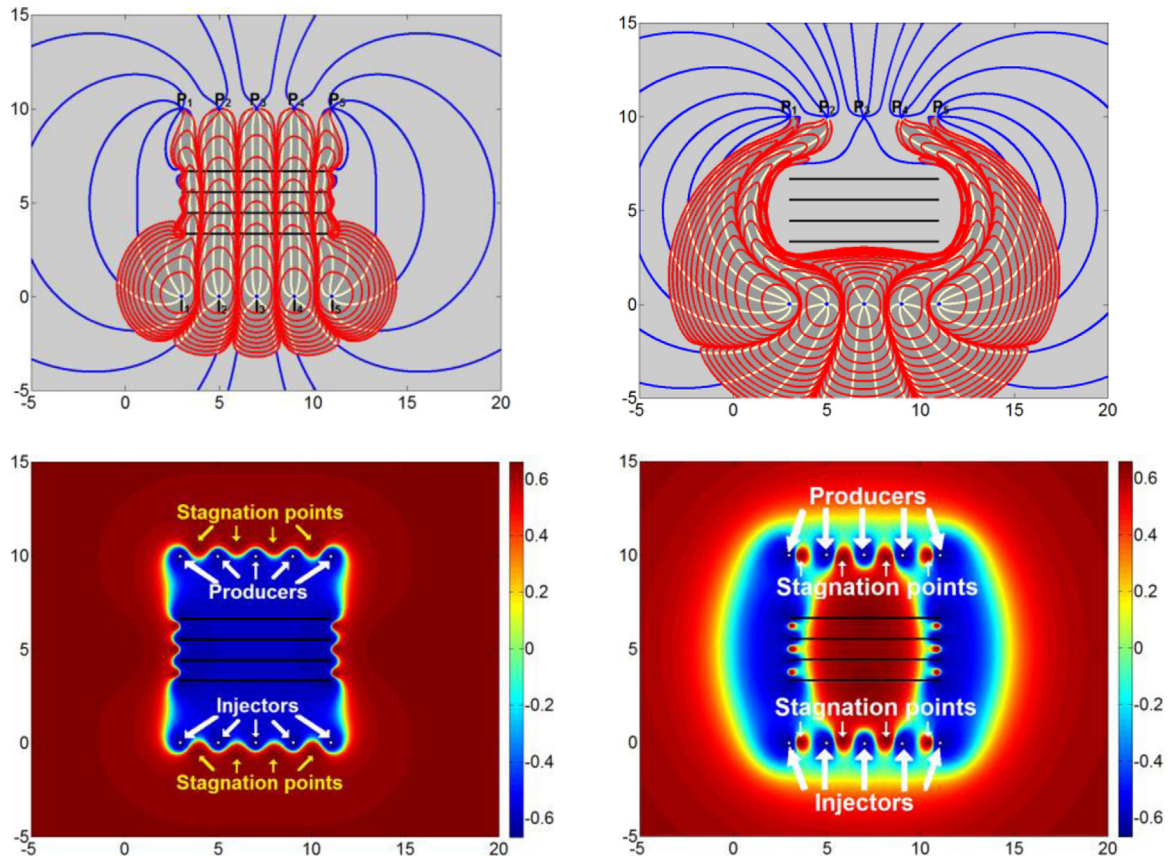$$\tan \alpha_1 / \tan \alpha_2 = \kappa_1 / \kappa_2 \tag{B3}$$

Fig. B3. Streamlines and Bernoulli pressure maps for high and low permeability zone using the analytical model with base case injector and producer strengths. Left: High permeability zone created by 4 line doublets (black lines) with unity strength per length. Orientation stimulates flow towards producers. Total non-dimensional time $t^*=4.5$, time between contours 0.5. Right: Low permeability zone created by 4 line doublets (black lines) with strength 8 and length 8. Orientation of doublet polarity is opposite to that in the left panel. Total non-dimensional run time $t^*=7$, and TOF contours are spaced for 0.5 time steps.
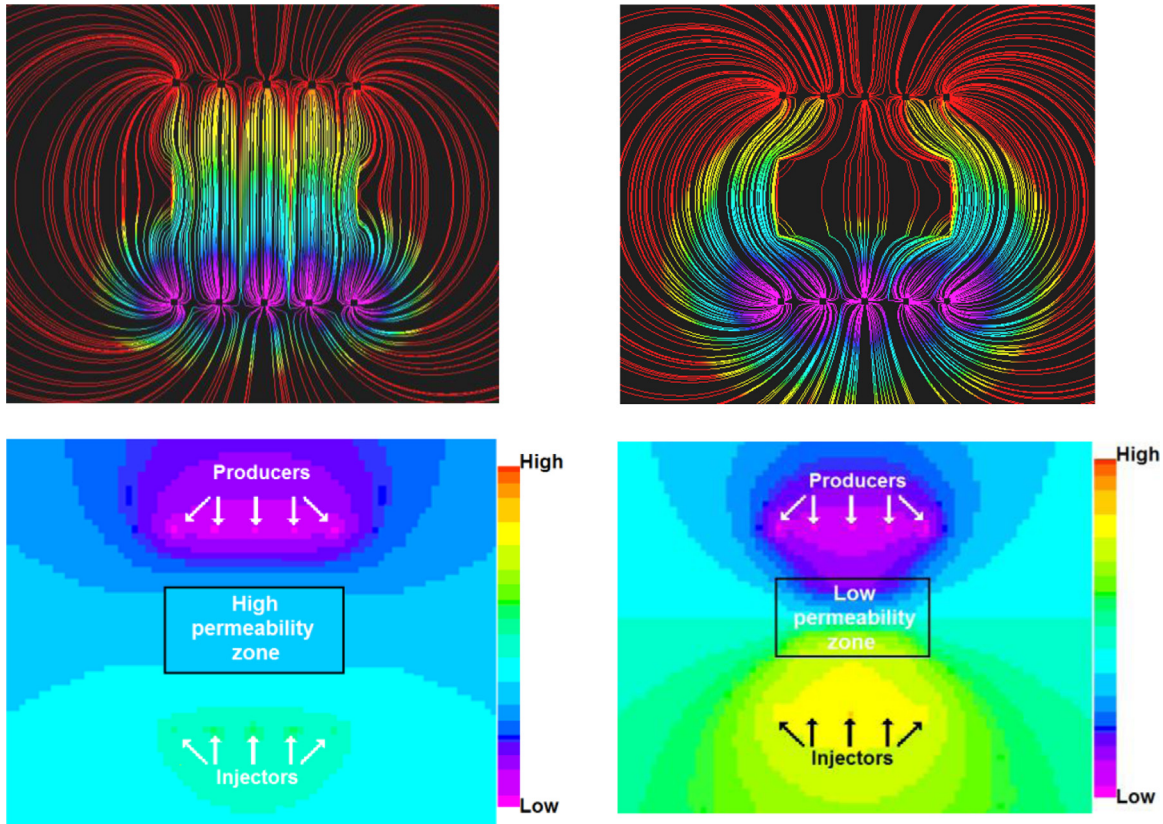
Fig. B4. Streamlines (top) and pressure maps (bottom) for high and low permeability zones generated using numerical solver software with base case injector and producer strengths. Reservoir ambient permeability is 100 mD. Left: High permeability zone of 1000 mD. Right: Low permeability zone of 10 mD.

This formula fits the angles observed in the numerical model (Fig. B4; Table B1), which allows us to empirically calibrate permeability zones created by superposing certain analytical elements like line doublets. The differences between 0.1 and the values in Table B1 likely are caused by inaccuracies in the flux and streamline calculations accumulating in ECLIPSE and DESTINY respectively.

Another basic insight abstracted from our modeling efforts is that streamline patterns for a particular set of initial reservoir properties and boundary conditions are dependent only on well rates and relative permeabilities. The actual time of flight (absolute travel times) along the streamlines are affected by such factors as porosity, but porosity changes that do not result in changes of permeability will not cause any shift of the streamline pattern. In other words, streamline patterns are fixed by well rates and permeabilities only. Such insight helps to properly interpret the meaning of the Kozeny–Carman equation that correlates permeabilities with porosity (Bear, 1972; Sato and Horne, 1993b):

$$\kappa(n) = \frac{cn^3}{(1-n)^2} \tag{B4}$$

with scaling parameter c [m^2] accounting for the combined effects of the pore space geometry and tortuosity of the capillary tubes. Eq. (B4) highlights that permeability is a macroscopic measure of the transmissivity that is the outcome of a particular physical pore

Table B1

Verification of the Refraction Law (in our case, $\frac{\kappa_1}{\kappa_2} = 0.1$).

Streamline#	1	2	3
Point 1	(111, 93.9791)	(130, 93.8815)	(130, 93.7347)
Point 2	(110.9097, 94)	(130.4543, 94)	(131.0158, 94)
Point 3	(110.2671, 95)	(130.9378, 95)	(131.5349, 95)
Permeability ratio	0.1487	0.1261	0.1356

space arrangement of capillary tubes accounting for the effects of porosity, tortuosity and any roughness of the capillary wells. Parameter c captures those effects and the relative values of c and n define the permeability. Identical permeabilities can occur with highly variable porosity. Streamtube positions are unaffected but velocities and reservoir pressures are higher when the porosity is lower for otherwise similar permeability distributions.

B2: ECLIPSE-based benchmarks

The analytical streamlines were benchmarked with an independent ECLIPSE-based streamline tracing algorithm, which also allowed comparison of time of flight for the advancing flood front. Three software packages were used during this process: ECLIPSE, DESTINY and Petrel. ECLIPSE and Petrel were designed by

Table B2

ECLIPSE-based model parameters.

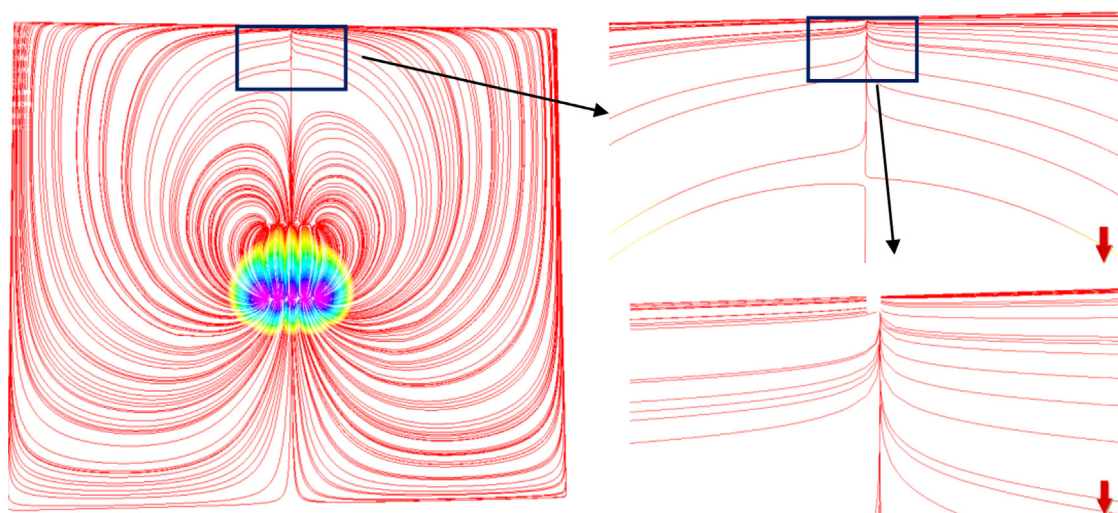| Parameters	Dimensions	Number of Grids	Porosity	Permeability	Injectors	Producers
Value	$250 \times 200 \times 1$	$250 \times 200 \times 1$	20	100	Water	Oil
Unit	ft		%	md	bbls/d	bbls/d

Fig. B5. Unstable flux solutions occur when larger grid dimensions are taken. This figure uses the same data as in Table B2 but $1000 \times 800 \times 1$ grid dimensions. The wrong flux solution causes severe errors in the streamline trajectories and TOF calculations. For example, in this figure, some streamlines end up in one "mystery" cell in the black box.

Schlumberger and DESTINY is designed by a research group at Texas A&M University (see acknowledgment). The base data used for the benchmark model is listed in Table B2. The model uses 5 injectors and 5 producers in a direct line drive arrangement geometrically similar to that used in the analytical model.

Based on the data provided in Table B2, we first designed the model in ECLIPSE data files. ECLIPSE is used to obtain output results such as pressures and flow rates on the 6 faces for each finite element cell. Next we run DESTINY, which can trace streamlines and calculate the TOF information. The streamline tracing algorithm is designed based on the method described in Datta-Gupta and King (2007). Then we upload the streamline tracing results in Petrel to visualize the streamlines and the pressure map.

We discovered that when we used larger dimensions, ECLIPSE delivered unstable pressure and flux results which became apparent from incongruent streamline patterns (Fig. B5). Such effects may impact the streamline tracing result and TOF calculation. There might be methods to avoid this and one should be careful when using dimensions with larger amounts of grid data.

References

Anderson, E.I., 2000. The method of images for leaky boundaries. Adv. Water Resour. 23 (5), 461–474. http://dx.doi.org/10.1016/S0309-1708(99)00044-5.

Anderson, E.I., Bakker, M., 2008. Groundwater flow through anisotropic fault zones in multiaquifer systems. Water Resour. Res. 44 (11). http://dx.doi.org/10.1029/2008WR006925.

Arps, J.J., 1945. Analysis of decline curves. Trans. AIME 160, 228–247.

Asheim, H. 1987. Optimal control of water drive. SPE J., SPE-15978-MS.

Asheim, H., 1988. Maximization of water sweep efficiency by controlling production and injection rates. In: SPE European Petroleum Conference, SPE-18365-MS, London.

Bakker, M., 2002. Two exact solutions for a cylindrical inhomogeneity in a multi-aquifer system. Adv. Water Resour. 25 (1), 9–18. http://dx.doi.org/10.1016/S0309-1708(01)00048-3.

Bakker, M., 2004. Modeling groundwater flow to elliptical lakes and through multi-aquifer elliptical inhomogeneities. Adv. Water Resour. 27, 497–506. http://dx.doi.org/10.1016/j.advwatres.2004.02.015 ().

Bakker, M., Anderson, E.I., 2003. Steady flow to a well near a stream with a leaky bed. Ground Water 41 (6), 833–840. http://dx.doi.org/10.1111/j.1745-6584.2003.tb02424.x.

Bakker, M., Nieber, J.L., 2004. Analytic element modeling of cylindrical drains and cylindrical inhomogeneities in steady two-dimensional unsaturated flow. Vadose Zone J. 3 (3), 1038–1049. http://dx.doi.org/10.2136/vzj2004.1038.

Barnes, R., Janković, I., 1999. Two-dimensional flow through large numbers of circular inhomogeneities. J. Hydrol. 226 (3–4), 204–210. http://dx.doi.org/10.1016/S0022-1694(99)00142-0.

Bear, J., 1972. Dynamics of Fluids in Porous Media. Elsevier, New York (repr. Dover, 1988).

Browning, B., Dobbs, W., Killough, J., Kumar, A., 2012. Coupled surface/subsurface simulation of a deepwater Gulf of Mexico field. Int. J. Eng. Appl. Sci. 1 (1), 23–46.

Bryson, A.E., Ho, Y.C., 1975. Applied Optimal Control: Optimization, Estimation and Control. Hemisphere-Wiley.

Brouwer, D.R., Jansen, J.D., 2004. Dynamic optimization of water flooding with smart wells using optimal control theory. SPE J. 9 (4), 391–402. http://dx.doi.org/10.2118/78278-PA, SPE-78278-PA.

Chorneyko, D.M., 2006. Real-time reservoir surveillance utilizing permanent downhole pressures – an operator's experience. SPE-103213-MS ⟨http://dx.doi.org/10.2118/103213-MS⟩.

Craig, J.R., 2006. The (almost) comprehensive analytic element biography ⟨http://www.civil.uwaterloo.ca/jrcraig/pdf/AEMBibliography.pdf⟩.

Datta-Gupta, A., King, M.K., 2007. Streamline Simulation: Theory and Practice. Texas: Textbook Series, SPE, Richardson.

Doyle, R.E., Wurl, T.M., 1971. Stream channel concept applied to waterflood performance calculations for multiwell, multizone, three-component cases. J. Pet. Technol. 23, pp. 373–380. http://dx.doi.org/10.2118/2653-PA, SPE-2653-PA.

Dupuit, J., 1863. Estudes Thèoriques et Pratiques sur le mouvement des Eaux dans les canaux dècouverts et à travers les terrains permèables, Second Edition Dunod, Paris.

Fokker, P.A., Verga, F., 2008. A semianalytic model for the productivity testing of multiple wells. SPE Reserv. Eval. Eng. 11 (3), 466–477. http://dx.doi.org/10.2118/94153-PA, SPE-94153-PA.

Fokker, P.A., Verga, F., Egberts, P., 2005. New semi-analytic technique to determine horizontal well PI in fractured reservoirs. SPE Res. Eval. Eng. 8 (02), 123–131. http://dx.doi.org/10.2118/84597-PA, SPE-84597-PA.

Forchheimer, P., 1886. Über die Ergiebigkeit von Brunnen- Anlagen und Sickerschlitzen. Z. Archit. Ing. -Ver. (Hann.) 32, 539–563.

Fyrozjaee, M.H., Y.C. Yortsos, 2006. Control of a displacement front in potential flow using flow rate partition. In: SPE Intelligent Energy Conference and Exhibition, SPE-99524-MS, Amsterdam.

Fyrozjaee, M.H., Y.C. Yortsos, 2011. Control of a displacement front in potential flow using flow-rate partition. Intelligent Energy Conference and Exhibition, 11–13 April, Amsterdam, The Netherlands. SPE-99524-MS. doi: 10.2118/99524-MS.

Goodier, J.N., 1936. Slow viscous flow and elastic deformation, London, Edinburgh Dublin Philos. Mag. J. Sci. Ser. 7 (22), 678–681.

Haitjema, H.M., 1995. Analytic Element Modeling of Groundwater Flow. Academic Press, San Diego.

Hazlett, R.D., Babu, D.K., Lake, L., 2007. Semi-analytical stream-function solutions on unstructured grids for flow in heterogeneous media. SPE J. 12 (2), 179–187. http://dx.doi.org/10.2118/95913-PA, SPE-95913-PA.

Higgins, R.V., Leighton, A.J., 1974. Matching calculated with actual waterflood performance by estimating some reservoir properties. J. Pet. Tech. 26 (05), 501–506. http://dx.doi.org/10.2118/4412-PA, SPE-4412-PA.

Irmay, S., 1964. Refraction d'un ecoulement a la frontiere separant deux milieux poreux anisotropes differents. Comptes Rendus Acad. Sci. 259, 509–511.

Janković, I., Barnes, R., 1999a. High-order line elements in modeling two-dimensional groundwater flow. J. Hydrol. 226 (3–4), 211–223. http://dx.doi.org/10.1016/S0022-1694(99)00140-7.

Janković, I., Barnes, R., 1999b. Three-dimensional flow through large numbers of spheroidal inhomogeneities. J. Hydrol. 226 (3–4), 224–233. http://dx.doi.org/10.1016/S0022-1694(99)00141-00149.

Jansen, J.D., 2011. Adjoint-based optimization of multi-phase flow through porous media – a review. Comput. Fluids 46 (1), 40–51. http://dx.doi.org/10.1016/j.compfluid.2010.09.039.

Jansen, J.-D., Brouwer, R., Douma, S.G., 2009. Closed Loop Reservoir Management. Paper SPE 119098 presented at the Reservoir Simulation Symposium. The Woodlands, Texashttp://dx.doi.org/10.2118/119098-MS.

Josseling de Jong, G., 1960. Singularity distributions for the anlaysis of multiple-fluid glow through porus media. J. Geophys. Res. 65 (11), 3739–3758.

Kraemer, S.R., 2003. The Maturity of Analytic Element Ground-Water Modeling as a Research Program (1980–2003). ⟨http://www.analyticelements.org/pubs/ste/kraemer_ste_2003.pdf⟩.

Kraemer, S.R., 2007. Analytic element ground water modeling as a research program (1980–2006). NGWA J. Ground Water 45 (4), 402–408.

Lake, L., Johns, R., Rossen, B., Pope, G., 2014. Fundamentals of Enhanced Oil Recovery. Society of Petroleum Engineers.

Møyner, O., Krogstad, S., Lie, K.A., 2015. The application of flow diagnostics for reservoir management. SPE J. 20 (2). http://dx.doi.org/10.2118/171557-PA (SPE-171557-PA).

Muskat, M., 1949a. Physical Principles of Oil Production. McGraw-Hill, New York.

Muskat, M., 1949b. The theory of potentiometric models. Transactions of the AIME, Part 1 vol. 179. Society of Petroleum Engineers, Richardson, Texas, pp. 216–221. http://dx.doi.org/10.2118/171557-PA.

Muskhelishvili, N.I., 1953. Some Basic Problems of the Mathematical Theory of Elasticity. Noordhoff, Groningen, p. 704.

Muskhelishvili, N.I., 1958. Singular Integral Equations. Noordhoff, Groningen.

Natvig, J.R., Lie, K.-A., 2008. Fast computation of multiphase flow in porous media by implicit discontinuous Galerkin schemes with optimal ordering of elements. J. Comput. Phys. 227 (24), 10108–10124. http://dx.doi.org/10.1016/j.jcp.2008.08.024 2008.

Olver, P., 2012. Complex Anal. Conform. Mapp. ⟨http://www.math.umn.edu/~olver/ln_/cml.pdf⟩

Pande, P.K., 2005. Business Realities and Challenges of Reservoir Simulation. Presented at the 8th International Forum on Reservoir Simulation, Stresa, Italy, 20–24 June.

Peters, E., Chen, Y., Leeuwenburgh, O., Oliver, D.S., 2013. Extended Brugge benchmark case for history matching and water flooding optimization. Comput. Geosci. 50, 16–24.

Peters, E., Arts, R.J., Brouwer, G.K., Geel, C.R., Cullikc, S., Dunlop, K.N.B., Vossepoel, F.C., Xu, R., Saram, P., Alhutali, A.H., Reynolds, A.C., 2010. Results of the Brugge benchmark study for flooding optimization and history matching. SPE Reserv. Eval. Eng. 13 (3), 391–405. http://dx.doi.org/10.2118/1109094-PA.

Pollock, D.W., 1988. Semi-analytical computation of path lines for finite-difference models. Groundwater 26 (6), 743–750.

Sato, K., 2015. Continuum Analysis for Practical Engineering. Springer, London (300 pp.).

Sato, K., Horne, R.N., 1993a. Perturbation boundary element method for heterogeneous reservoirs: Part 1. Steady-state flow problems. SPE Form. Eval. 8 (4), 206–314. http://dx.doi.org/10.2118/25299-PA, SPE-25299-PA.

Sato, K., Horne, R.N., 1993b. Perturbation boundary element method for heterogeneous reservoirs: Part 2. Transient flow problems. SPE Form. Eval. 8 (4), 315–322. http://dx.doi.org/10.2118/25300-PA, SPE-25300-PA.

Sato, K., Watanabe, Y., 2004. Treatment of Neumann boundaries in complex variable boundary element method. Common. Numer. Method Eng. 20, 119–132.

Schmid, D.W., Podladchikov, Y.Y., 2003. Analytical solutions for deformable elliptical inclusions in general shear. Geophys. J. Int. 155 (2003), 269–288.

Smalley, P.C., Ross, B., Brown, C.E., Moulds, T.P., Smith, M.J., 2009. Reservoir technical limits: a framework for maximizing recovery from oil fields. SPE Res. Eval. Eng. 12 (4), 6120–6629. http://dx.doi.org/10.2118/109555-PA, SPE-109555-PA.

Strack, O.D.L., 1981a. Flow in aquifers with clay laminae 1. The comprehensive potential. Water Resour. Res. 17 (4), 985–992.

Strack, O.D.L., 1981b. Flow in aquifers with clay laminae 2. Exact solutions. Water Resour. Res. 17 (4), 993–1004.

Strack, O.D.L., 1989. Groundwater Mechanics. Prentice-Hall, Englewood Cliffs, New Jersey.

Strack, O.D.L., 1999. Principles of the analytic element method. J. Hydrol. 226 (3–4), 128–138. http://dx.doi.org/10.1016/S0022-1694(99)00144-4.

Strack, O.D.L., 2003. Theory and applications of the analytic element method. Rev. Geophys. 41 (2), 1005. http://dx.doi.org/10.1029/2002RG000111.

Strack, O.D.L., 2006. The development of new analytic elements for transient flow and multi-aquifer flow. Ground Water 44 (1), 91–98. http://dx.doi.org/10.1111/j.1745-6584.2005.00148.x.

Strack, O.D.Lu, Haitjema, 1981a. Modeling double aquifer flow using a comprehensive potential and distributed singularities 1. Solution for homogeneous permeability. Water Resour. Res. 17 (5), 1535–1549.

Strack, O.D.L., Haitjema, 1981b. Modeling double aquifer flow using a comprehensive potential and distributed singularities 2. Solution for inhomogeneous permeabilities. Water Resour. Res. 17 (5), 1551–1560.

Sudaryanto, B., Yortsos, Y.C., 2001. Optimization of displacements in porous media using rate control. SPE Annu. Tech. Conf. Exhib. (SPE71509)

Suribhatla, R., Bakker, M., Bandilla, K., Janković, I., 2004. Steady two-dimensional groundwater flow through many elliptical inhomogeneities. Water Resour. Res. 40 (4). http://dx.doi.org/10.1029/2003WR002718.

Unneland, T., Hauser, M. 2005. Real-time asset management: fromvision to engagement – an operator's experience. Paper SPE 96390 presentedat the SPE Annual Technical Conference and Exhibition, Dallas, 9–12 October. doi: 10.2118/96390-MS.

Weijermars, R., Schmeling, H., 1986. Scaling of Newtonian and non-Newtonian fluid dynamics without inertia for quantitative modeling of rock flow due to gravity (including the concept of rheological similarity). Phys. Earth Planet. Inter. 43 (4), 316–330. http://dx.doi.org/10.1016/0031-9201(86)90021-X.

White, F.M., 2011. Fluid Mechanics. McGraw Hill, New York.

Zandvliet, M.J., 2008. Model-based Lifecycle Optimization of Well Locations and Production Settings in Petroleum Reservoirs (Ph.D dissertation), Technische Universiteit Delft, Delft (April 2008).

Zhang, Y., Yang, C., King, M.J., Datta-Gupta, A., Fast-Marching Methods for Complex Grids and Anisotropic Permeabilities: Application to Unconventional Reservoirs, SPE-163637-MS presented at the S.P.E. Reservoir Simulation Symposium held in The Woodlands, Texas USA, 18 February 2013.